Grounding line migration in an adaptive mesh ice sheet model

Gladstone, R M ; Lee, V ; Vieli, Andreas ; Payne, A J

Abstract: Grounding line migration is a key process affecting the stability of marine ice sheets such as the West Antarctic ice sheet. Recent studies have shown that ice sheet models employing a fixed spatial grid (such as are commonly used for whole ice sheet simulations) cannot be used to solve this problem in a robust manner. We have developed a one-dimensional (vertically integrated) "shelfy stream" ice sheet model that employs the adaptive mesh refinement (AMR) technique to bring higher resolution to spatially and temporally evolving subregions of the model domain. A higher-order solver, the piecewise parabolic method (PPM), is used to compute the thickness evolution. Both AMR and PPM extend readily to greater than one dimension and could be used in full ice sheet simulations. We demonstrate that this approach can bring improvements in terms of accuracy and consistency in both grounded ice sheet and ice stream/ice shelf simulations, given the appropriate choice of refinement criteria. In particular, we demonstrate that AMR, in conjunction with a parameterization for subgrid scale grounding line position, can produce predictions of grounding line migration.

DOI: https://doi.org/10.1029/2009JF001615

Grounding line migration in an adaptive mesh ice sheet model

R. M. Gladstone,[1] V. Lee,[1] A. Vieli,[2] and A. J. Payne[1]

Received 18 December 2009; revised 28 May 2010; accepted 23 July 2010; published 27 October 2010.

[1] Grounding line migration is a key process affecting the stability of marine ice sheets such as the West Antarctic ice sheet. Recent studies have shown that ice sheet models employing a fixed spatial grid (such as are commonly used for whole ice sheet simulations) cannot be used to solve this problem in a robust manner. We have developed a one-dimensional (vertically integrated) "shelfy stream" ice sheet model that employs the adaptive mesh refinement (AMR) technique to bring higher resolution to spatially and temporally evolving subregions of the model domain. A higher-order solver, the piecewise parabolic method (PPM), is used to compute the thickness evolution. Both AMR and PPM extend readily to greater than one dimension and could be used in full ice sheet simulations. We demonstrate that this approach can bring improvements in terms of accuracy and consistency in both grounded ice sheet and ice stream/ice shelf simulations, given the appropriate choice of refinement criteria. In particular, we demonstrate that AMR, in conjunction with a parameterization for subgrid scale grounding line position, can produce predictions of grounding line migration.

Citation: Gladstone, R. M., V. Lee, A. Vieli, and A. J. Payne (2010), Grounding line migration in an adaptive mesh ice sheet model, *J. Geophys. Res.*, *115*, F04014, doi:10.1029/2009JF001615.

1. Introduction

[2] The potential of marine ice sheets such as the West Antarctic Ice Sheet (WAIS) to undergo rapid collapse in response to climate change (sometimes referred to as "marine ice sheet instability"), and the possible resulting sea level rise, has been discussed from the 1970s to the present day [e.g., *Mercer*, 1978; *Vaughan*, 2008]. However, as yet predictions of the timescale over which the WAIS might collapse, or even whether it will collapse for a given climate change scenario, have not been made. A more extended introduction to marine ice sheet instability and recent developments in the area is given by *Katz and Worster* [2010].

[3] In order to make predictions about the stability and rate of collapse of marine ice sheets, computer models of ice sheet behavior are needed, and these models must include a realistic representation of the motion of the grounding line. *Vieli and Payne* [2005] demonstrated that the grounding line in models where computations are carried out at fixed horizontal locations exhibits very strong resolution-dependent behavior, and hypothesized that at sufficiently high resolution this could be overcome. Analytic and numerical modeling studies of the transition (from grounded to floating) zone [*Schoof*, 2007] indicate that some form of adaptivity is vital in numerical models of grounding line migration.

[4] A moving grid model in which an equation for grounding line migration rate is solved, and the grid is stretched such that a grid point always lies directly at the simulated grounding line position, shows less dependency on resolution than fixed grid models [*Vieli and Payne*, 2005]. However, the moving grid approach of *Vieli and Payne* [2005] would be very difficult to implement in a full ice sheet model and also too computationally expensive to be used for the whole of Antarctica.

[5] *Katz and Worster* [2010] present a 3-D model for marine ice sheets. The model makes use of a grid transformation which allows the grounding line to move whilst exactly overlying grid points, a feature in common with the moving grid approach. Their model has several limitations preventing it from being usable in quantitative predictive studies of real world marine ice sheets in its current state. However, it has been used with idealized bedrock configurations to show that an up sloping bedrock profile along a flowline does not necessarily preclude stable steady grounding line positions. The surrounding bedrock configuration can in some cases (they demonstrate a narrow valley example) cause stability. Hence in order to properly assess the stability of marine ice sheets a model with at least two spatial dimensions is needed.

[6] A form of adaptive mesh refinement based on a fixed grid model, in which higher resolution is used in the vicinity of the grounding line within a variable grid size domain, has been used in a 2-D (along flow and vertical coordinates) full Stokes ice sheet model [*Durand et al.*, 2009a]. This approach enables much higher resolution at the grounding line than would otherwise be possible. Grounding line behavior appears to be converging as resolution near the grounding line is increased, but it was not possible to run at a sufficiently high resolution to conclude whether complete convergence can occur [*Durand et al.*, 2009b].

[1]Bristol Glaciology Centre, School of Geographical Sciences, Bristol University, Bristol, UK.
[2]Department of Geography, Durham University, Durham, UK.

0148-0227/10/2009JF001615

Table 1. Summary of Models Used in This Study[a]

Model Name	Description
FGSH	fixed grid ice sheet model
FGSH_PPM	fixed grid ice sheet model using piecewise parabolic method for thickness
AGSH	adaptive grid ice sheet model
MGSTXX	moving grid ice stream model
FGSTSF	fixed grid ice stream/shelf model
AGSTSF	adaptive grid ice stream/shelf model
AGSTSF_GF	adaptive grid ice stream/shelf model with feedback of grounding line position to lower refinement levels
FGSTSF_GI	fixed grid ice stream/shelf model using linear interpolation to determine grounding line position
AGSTSF_GIF	adaptive grid ice stream/shelf model with feedback of grounding line position to lower refinement levels and linear interpolation to determine grounding line position

[a]Note that the PPM thickness solver is used in all the STSF models.

[7] *Goldberg et al.* [2009] implemented two forms of adaptivity in two horizontal dimensions; a moving mesh (without explicit grounding line tracking, i.e., the grounding line does fall in between grid cells) and adaptive refinement (somewhat similar to *Durand et al.* [2009a]), and used these approaches to investigate the impacts of ice shelf buttressing. They found that buttressing had a significant impact on grounding line behavior.

[8] The current study uses a form of adaptive mesh refinement (AMR) in which higher-resolution nested grids (called patches) are created and evolved at run time in order to bring higher resolution to where it is needed (e.g., near the grounding line in the case of marine ice sheet instability studies). This approach has 4 main advantages: it is expected to scale easily to two- or three-dimensional full ice sheet models (using third party software such as CHOMBO [*Meglicki et al.*, 2007]); the higher time step required for the higher resolutions need not be used over the whole model domain (thus improving efficiency); existing fixed grid solvers can be used without further modifications to evolve the solution on each patch independently; and multigrid techniques which speed up convergence of iterative methods can more easily be integrated in the model. The current study tests this approach to adaptivity in a 1-D flowline model as a proof of concept for applying this approach in more than one dimension. This model is cheap to run and finer resolution can be achieved than in the adaptive and moving grid studies mentioned above.

[9] *Pattyn et al.* [2006] showed that improvements to grounding line modeling with fixed grid models could be made using a parameterization for subgrid scale determination of grounding line position based on linear interpolation of a function of ice thickness and bed rock depth. *Pollard and DeConto* [2009] used the parameterizations of *Pattyn et al.* [2006] and *Schoof* [2007] to calculate grounding line position and cross-grounding line fluxes in a multimillion year simulation or the entire Antarctic ice sheet. However, robust experiments to investigate resolution dependency using the parameterization have not yet been carried out. The current study uses a similar approach, linearly interpolating both bed rock depth and ice sheet thickness over the first floating grid cell in order to parameterize the grounding line position at subgrid scale precision.

[10] Improving ice sheet models in general means not only increasing the complexity of their dynamics using higher-order models, but also improving the numerical schemes to capture more realistic flow features. By using higher-order models, the stresses and thickness of the ice sheet are described by a system of coupled nonlinear equations that cannot be combined into a single equation as is the case for a simple zero order model [*Hutter*, 1983; *Hindmarsh and Payne*, 1996]. The evolution equation for the ice thickness has a hyperbolic form and as such simple numerical schemes are either highly diffusive, unstable or introduce spurious oscillations. Hyperbolic equations are common in engineering and science, and many schemes have been developed to mitigate these numerical problems. One such scheme, the piecewise-parabolic method (PPM) [*Colella and Woodward*, 1984] will be introduced into the ice sheet model in this study. It is an explicit up-winding finite differencing scheme that allows for nonuniform grid spacing that is at least third-order accurate in space and time. It has two parts: spatial interpolation and advection. Firstly, interpolation of variables is carried out using parabolae, which allows good representation of smooth spatial gradients. The piecewise-parabolic interpolation function is modified such that its slope is increased where gradients are steep, and oscillations are suppressed by applying a monotonicity constraint. Secondly, high temporal accuracy is achieved by exploiting the exact solution to the linear first-order wave equation to advect the interpolated variable forward in time.

[11] This study introduces two existing numerical techniques that have yet to be widely adopted by the glaciology community: the PPM method for thickness evolution (Appendix A), and AMR (Appendix B). The ice flow models are described in section 2. Results from a simple ice sheet experiment using the shallow ice approximation are shown in section 3. Results from ice shelf/ice stream experiments, in which the use of a grounding line parameterization is also investigated, are shown in section 4, which goes on to look at the impact of refinement parameters on the results. How refinement parameters can be intelligently managed to reduce error, along with the applicability of adaptivity to full ice sheet models with more than one spatial dimension, are discussed in section 5.

2. Model Description

[12] The models presented here build on the fixed grid model FGSTSF (see Table 1) presented by *Vieli and Payne* [2005]. They are all vertically integrated (i.e., vertical shearing cannot be represented). Changes/additions to that model include the use of adaptivity (Appendix B), the PPM solver for thickness (Appendix A) and a linear interpolation technique for determining grounding line position subgrid scale accuracy (section 2.2.4).

2.1. Governing Equations

[13] Conservation of mass for ice sheets, streams and shelves in the case of a single dimension, x, is given by

$$\frac{\partial H}{\partial t} + \frac{\partial (uH)}{\partial x} = a, \tag{1}$$

where u is the vertically integrated horizontal velocity, a is the net surface accumulation and H is the ice thickness.

2.1.1. Ice Sheet Flow

[14] For ice sheet flow the shallow ice approximation (SIA [*Hutter*, 1983; *Paterson*, 1994]) gives

$$u = CH^{n+1}\left(\frac{\partial s}{\partial x}\right)^n, \tag{2}$$

where n is Glen's flow law exponent and s is the surface height of the ice sheet relative to sea level. The constant C is given by

$$C = \frac{2}{n+2}A(\rho g)^n, \tag{3}$$

where A is the rate factor, ρ the density of ice and g the acceleration due to gravity.

2.1.2. Ice Stream/Shelf Flow

[15] Ice stream and shelf flow is given (as by *Vieli and Payne* [2005]) by

$$2\frac{\partial}{\partial x}Hv\frac{\partial u}{\partial x} - \beta^2 u = \rho g H\frac{\partial s}{\partial x}, \tag{4}$$

where β^2 is a positive friction coefficient and v is the vertically averaged effective viscosity. Thus the drag at the base is linear with the vertically integrated velocity, u. Experiments with a nonlinear drag law (drag force proportional to $u^{\frac{1}{3}}$) show qualitatively similar behavior and are not presented here. For the ice shelf, basal drag is removed by setting $\beta^2 = 0$. v is given by

$$v = A^{-1/n}\left[\left(\frac{\partial u}{\partial x}\right)^2\right]^{(1-n)/2n}. \tag{5}$$

2.1.3. Boundary Conditions

[16] In the case of the boundary lying at the edge of a grounded ice sheet, a zero thickness boundary condition is used. Where the boundary lies at the ice divide, symmetry about the ice divide in the direction of the flowline is assumed, implying zero flux and zero surface slope at the divide. Where the boundary lies at the floating ice front, the longitudinal stress is balanced by the hydrostatic pressure of the ocean water [*Vieli and Payne*, 2005; *Paterson*, 1994] which gives

$$\left.\frac{\partial u}{\partial x}\right|_{x=l} = A\left[\frac{1}{4}\rho g\left(1-\frac{\rho}{\rho_w}\right)\right]^n H^n, \tag{6}$$

where ρ_w is the density of sea water and l is the position of the ice shelf front.

2.2. Numerical Models

[17] Two ice sheet regimes, a wholly grounded ice sheet and a partially floating ice stream/ice shelf system, are studied. A brief summary of the models used in this study is given in Table 1. The abbreviations used to construct the model names shown in Table 1 (following the convention of *Vieli and Payne* [2005]) are given in parentheses in this section.

[18] The grounded ice sheet models that do not use the Piecewise Parabolic Method (PPM) for thickness evolution (namely FGSH and AGSH) are solved as a single equation. The equation is obtained by substituting equation (2) into the thickness equation (1) and reformulating it into a diffusion-type equation. This is spatially discretized on a staggered grid (i.e., fluxes are calculated on a grid spatially offset by $\Delta x/2$ from the thickness grid) using second-order central differences and marched forward in time using the Crank-Nicolson method (grid type 1 of *Hindmarsh and Payne* [1996]).

[19] The grounded ice sheet model utilizing the PPM (FGSH_PPM) solves equations (1) and (2) separately. The ice stream/shelf (STSF) models solve equations (1) and (4) with boundary condition 6. In both of these cases the system evolves using a marching scheme with a two-step procedure on a staggered grid. At each time step velocity is constructed using second-order finite differences of the thickness from the previous time step. The calculated velocity is used in the PPM scheme, which marches the ice thickness forward in time (section 2.2.2). All fixed grid (FG) and adaptive grid (AG) ice stream/ice shelf (STSF) models use the PPM for thickness evolution.

[20] A parameterization for grounding line position (present in models FGSTSF_GI and AGSTSF_GIF), and a description of how the AMR technique can be modified to better represent grounding line migration (used in models AGSTSF_GF and AGSTSF_GIF), are described in section 2.2.4. Results are also presented from the moving grid ice stream (MGSTXX) model of *Vieli and Payne* [2005]. This model has been shown to produce more consistent results than the fixed grid models [*Vieli and Payne*, 2005] and is shown here for comparison. The MGSTXX allows the grid points to move such that the grounding line always directly overlies a grid point. See *Vieli and Payne* [2005] for a full description.

2.2.1. Grid and Variable Arrangement

[21] All models other than FGSH and AGSH calculate velocity separately from thickness on a staggered (offset by *Deltax*) grid. The PPM scheme (Appendix A) used to solve for thickness uses N zones, and the velocity solver uses a staggered grid with N grid points. In the interior of the domain both are equivalent. At the edges of the domain the requirements differ, however, with the velocity solver requiring thickness values and the PPM requiring velocity. This is resolved in the thickness solver by positioning the centre of the zone at the edge of the domain on the boundary and adding velocity on the outer zone edge. This means that the PPM domain is half a grid cell larger at each end and has two more velocity points than the grid from the velocity solver. The values of the extra velocities are determined by the boundary conditions of the problem (section 2.2.3).

2.2.2. Using the PPM to Solve for Ice Thickness

[22] The calculated velocities are used by the PPM to calculate time averaged ice fluxes over the subsequent time step, $\overline{\phi}$, which are then used to evolve the thickness profile, H. From equation (A8), the following expression for flux calculation is derived

$$\overline{\phi}_{i+\frac{1}{2}} = \begin{cases} u_{i+\frac{1}{2}} f^H_{i+\frac{1}{2},L}\left(u_{i+\frac{1}{2}}\Delta t\right) & \text{if } u_{i+\frac{1}{2}} \geq 0 \\ u_{i+\frac{1}{2}} f^H_{i+\frac{1}{2},R}\left(-u_{i+\frac{1}{2}}\Delta t\right) & \text{otherwise,} \end{cases} \tag{7}$$

where $u_{i+\frac{1}{2}}$ and $\overline{\phi}_{i+\frac{1}{2}}$ are the velocity and time averaged flux, respectively, through the right hand edge of the ith zone, and Δt is the time step (which satisfies the condition $\max_i u_i + \frac{1}{2}\Delta t \leq \min_i \Delta x_i$). $f^H_{i+\frac{1}{2},L}$ and $f^H_{i+\frac{1}{2},R}$ are the averaging functions of the interpolated thickness described in section 1.1.2, equations (A6) and (A7). The ice thickness H is then marched forward in time using the following explicit, finite difference scheme (derived from equation (1)),

$$H_i^{k+1} = H_i^k - \frac{\left(\overline{\phi}_{i+\frac{1}{2}} - \overline{\phi}_{i-\frac{1}{2}}\right)}{\Delta x_i}\Delta t + a\Delta t, \tag{8}$$

where Δx_i is the zone width.

2.2.3. Boundary Condition Implementation

[23] The implementation of boundary conditions for the edge of the grounded ice sheet, the ice divide and the ice shelf front are all handled differently, and are described here. Most of the models used in this study require boundary conditions to be implemented separately for the velocity and thickness solvers. The PPM in particular needs extra information at the boundaries in order to populate the ghost zones (as described in section 1.1.3). Where AMR is used, internal boundary conditions (i.e., at patch boundaries where the patch does not reach the edge of the base grid) need to be specified (section 2.2.3.4).

2.2.3.1. Grounded Ice Sheet Boundary Conditions

[24] A Dirichlet (or first-type) boundary condition of zero thickness is used for the single equation models FGSH and AGSH. In the FGSH_PPM model, a zero velocity Dirichlet boundary condition is used for the velocity calculation. For the PPM, the zero thickness boundary condition is implemented through setting the ghost zone values to zero. The widths of the ghost zones are set to the value of the zone at the boundary. The extra velocity on the outer edge of the boundary zone is set to zero to ensure zero flux. At the end of the time step the thickness in the boundary zone is reset to the fixed value. The boundary condition is enforced again because there may be a small drift in the calculated thickness in the boundary zone if the parabolic interpolation functions cannot perfectly match the discrete thickness values.

2.2.3.2. Ice Divide Boundary Conditions

[25] The ice divide (present in all STSF models, Table 1) is assumed to overlie the first velocity point, $u_{\frac{1}{2}}$ (which lies on the staggered grid). This means that the ice divide is effectively a distance of $\Delta x/2$ from the left boundary of the domain. A zero velocity Dirichlet condition is used for the velocity calculation at the ice divide.

[26] The PPM thickness solver requires velocity to be defined on an additional velocity point $u_{\left(-\frac{1}{2}\right)}$ lying outside the domain, immediately to the left of the left most thickness grid point, h_0. By symmetry about the ice divide the following are used for this velocity value and for the thickness values in the ghost zones:

$$\begin{aligned} u_{\left(-\frac{1}{2}\right)} &= -u_{\left(1\frac{1}{2}\right)} \\ H_{(1-i)} &= H_{(i)}, \quad i \in \{1,2,3\} \end{aligned}.$$

2.2.3.3. Ice Shelf Front Boundary Conditions

[27] A Neumann (or second-type) boundary condition is formulated using the force balance equation (6) for the velocity calculation. In the PPM thickness solver, the ice shelf front is treated as an open boundary where ice is allowed to flow freely from the domain. At an open boundary the thickness gradient is assumed to be zero. The width and value of thickness in each ghost zone are equal to those of the boundary zone. The required extra velocity value ($u_{\left(l+\frac{1}{2}\right)}$ where l indicates the position of the shelf front boundary) outside the domain is set using linear extrapolation (note grid spacing is constant here) of the velocity near the boundary:

$$u_{\left(l+\frac{1}{2}\right)} = 2u_{\left(l-\frac{1}{2}\right)} - u_{\left(l-\frac{3}{2}\right)}. \tag{9}$$

2.2.3.4. Internal Boundary Conditions

[28] Where simulations using adaptivity contain patches that do not coincide with the edge of the base domain, suitable internal boundary conditions must be used. The values used in internal boundary conditions always come from the parent patch.

[29] For the adaptive grid grounded ice sheet model (AGSH), two different boundary conditions have been used in this study. Firstly, a Dirichlet thickness boundary condition in which the thickness value at the internal boundary is taken directly from the parent patch. Secondly, a Neumann boundary condition has been used, in which fluxes are prescribed. The flux values needed to set up the condition are calculated using linear interpolation from the parent patch.

[30] For the ice stream/ice shelf simulations (the AGSTSF models), a Dirichlet velocity boundary condition is calculated by linear interpolation from the parent patch for the velocity solver. For the thickness solver (PPM), thickness and velocity at the boundary, in addition to thickness in the ghost zones, are set from the parent using linear interpolation where needed. A more elegant solution would be to make use of the PPM's ability to cope with varying grid resolution by taking the parent thickness values directly and use the parent resolution for width of the ghost zones, however this would in practice slightly reduce efficiency by requiring increased patch sizes (the parent patch would be required to extend further beyond the child patch than with linear interpolation), and in practice there is not a significant gain in terms of accuracy; our experiments (not shown) have shown thickness evolution within a patch to be sensitive to the thickness value in the first ghost zone, but relatively insensitive to thickness values in further ghost zones.

2.2.4. Grounding Line Position

[31] Traditionally, fixed grid models determine grounding line position using the floatation condition at each thickness grid point (equation (9)) [*Vieli and Payne*, 2005], and effectively constraining the grounding line to be at the position of the last grounded grid point. In order to improve upon this assumption, *Pattyn et al.* [2006] parameterized the grounding line position at subgrid resolution using linear interpolation of a function f of thickness and bedrock elevation over the grid cell containing the grounding line to determine an exact position at which the floatation condition is met. Based on the floatation condition, f is given by

$$f = \frac{\rho_w b}{\rho H}, \tag{10}$$

Table 2. Forcing Parameters, Physical Parameters, and Constants

Parameter	Units	Grounding Line Experiments	Ice Sheet Experiments
Rate factor, A	$Pa^{-3}\ yr^{-1}$	9.2×10^{-18}	1.0×10^{-16}
Corresponding temperature[a]	C	−15	−50
Flow law exponent, n		3	3
Drag coefficient, β^2	Pa s m^{-1}	5×10^9	
Bedrock		down sloping	flat
Net accumulation, a	m yr^{-1}	0.3	0.3
Ice density, ρ	kg m^{-3}	910	910
Ocean water density, ρ_w	kg m^{-3}	1028	

[a]Approximate effective ice temperature, derived from the rate factor.

where b is the bedrock depth below sea level. In the current study we take the simpler approach of linearly interpolating both thickness and bedrock depth over the grid cell containing the grounding line. These interpolations are independent from each other. If i is the last grounded grid point, interpolated thickness is given by

$$H_g = H_i\left(1 - \frac{x_g - x_i}{\Delta x}\right) + H_{i+1}\left(\frac{x_g - x_i}{\Delta x}\right), \tag{11}$$

where x_g and x_i are the distances of the grounding line and last grounded grid point, respectively, from the edge of the domain, and H_g is grounding line thickness. A similar expression is derived for bedrock depth at the grounding line, b_g, and these are solved for x_g along with the floatation condition at the grounding line,

$$\rho H_g = \rho_w b_g. \tag{12}$$

This linear thickness grounding line parameterization is used in models FGSTSF_GI and AGSTSF_GIF (where GI stands for grounding line interpolation).

[32] The grounding line position impacts the time evolution of the model by scaling the basal drag coefficient in the grid cell containing the grounding line. When resolving the force balance in the grid cell containing the grounding line (i.e., at position $i + \frac{1}{2}$ where the grounding line, x_g, lies between x_i and x_{i+1}), the drag coefficient β^2 is replaced with β_g^2 given by

$$\beta_g^2 = \beta^2 \times \frac{(x_g - x_i)}{\Delta x} x_i < x_g < x_{i+1}. \tag{13}$$

[33] Unmodified AMR involves a one way flow of information up through the hierarchy, the boundary conditions of each patch being provided by the parent patch. Hence the grounding line accuracy at any given refinement level is to some extent limited by the grounding line accuracy at the next lower level; if the grounding line is inaccurate at level κ then this inaccuracy will be conveyed via the boundary conditions given to the patch at level $\kappa + 1$.

[34] In order to overcome this limitation, we have implemented, in models AGSTSF_GF and AGSTSF_GIF, the use of $x_g(\kappa_{\max})$ instead of $x_g(\kappa)$ to give grounding line position in each patch. In other words, the grounding line position is calculated only at the highest refinement level, and all patches and the base grid use this value. This impacts via β^2 as above, equation (13).

3. Grounded Ice Sheet Experiments

[35] Before considering grounding line migration we assess the accuracy of models FGSH, FGSH_PPM and AGSH (Table 1) for the case of a grounded ice sheet. This is done by comparing their steady state thickness profiles against an analytic solution for a grounded ice sheet with zero thickness boundary conditions [*Vialov*, 1958]. For the model AGSH which uses adaptivity this setup provides a test for the truncation error estimation adaptivity criterion (Appendix B2.1).

[36] The domain size is 1500 km, base grid resolution is defined by Δx = 50 km and Δt = 4 yr, and the bed rock is flat. Net accumulation, a, is constant both temporally and spatially. At the boundaries of the base domain zero thickness is prescribed. Each experiment is run to steady state. See Table 2 for a summary of parameter values.

[37] The AGSH model uses refinement factor Δ_κ = 2, giving spatial resolutions of 25 km, 12.5 km and 6.25 km for patches at refinement levels 2, 3 and 4 respectively. Refinement frequency is 20. The adaptivity criterion for AGSH is estimated truncation error (described in section 2.2.1). AGSH simulations were initially carried out using thickness internal boundary conditions. Further simulations were carried out using flux internal boundary conditions (section 2.2.3.4).

[38] These experiments consist of spin up from zero initial thickness to steady state. The validation metric in these experiments is thickness error in meters calculated as a simple difference against the analytic steady state solution. The steady state solution [*Vialov*, 1958] is:

$$H = H_d\left(1 - \left|\frac{L - 2x}{L}\right|^{\frac{4}{3}}\right)^{\frac{3}{8}}, \tag{14}$$

where L is the length of the ice sheet and H_d is the thickness at the ice divide given by

$$H_d = \left(\frac{20\,a}{A}\right)^{\frac{1}{8}}\left(\frac{1}{\rho g}\right)^{\frac{3}{8}}\left(\frac{L}{2}\right)^{\frac{1}{2}}. \tag{15}$$

The FGSH steady state thickness and error profiles are shown in Figure 1. The errors become large near the margins where the gradient is steep.

[39] Use of adaptivity reduces the errors (Figure 1b) with both thickness (Dirichlet) and flux (Neumann) internal boundary conditions. Use of the thickness boundary condition forces the patch boundaries to inherit the thickness truncation error from the parent patch (Figure 1b, dark gray curve). The flux internal boundary condition allows the patch thickness to evolve independently, and reduces the error more than the thickness boundary condition (Figure 1b, black curve). Independent of the internal boundary conditions it can be seen that the estimated truncation error based refinement criterion effectively identifies the regions in which errors are greatest, making the adaptivity an efficient way to reduce errors in this case.

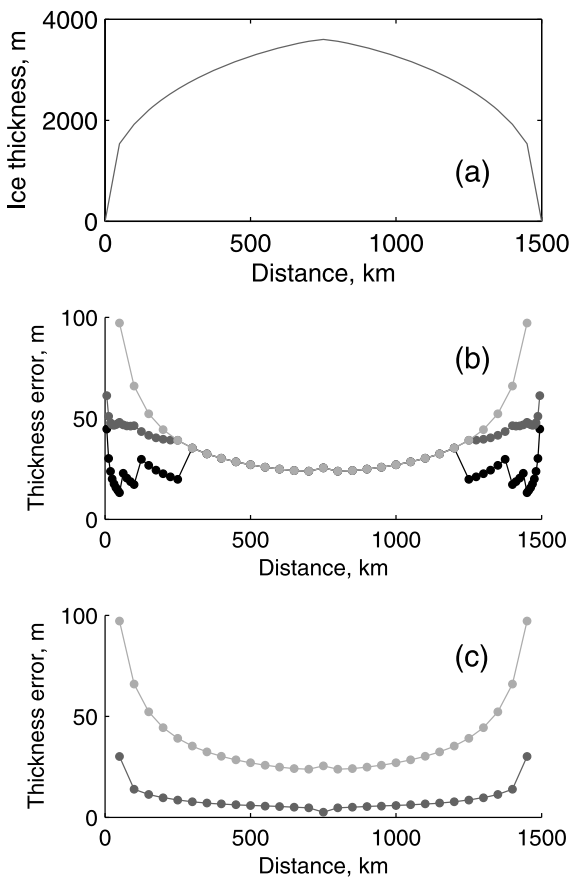

Figure 1. Grounded ice sheet model results. (a) Steady state ice thickness from the fixed grid ice sheet (FGSH) model. The absolute error (i.e., magnitude of the difference between modeled and analytic thickness) for (b) AGSH with $\kappa = 4$ for both thickness (dark gray) and flux (black) internal boundary conditions and (c) FGSH_PPM (dark gray). The absolute error of FGSH is shown in light gray in both Figures 1b and 1c.

[40] Implementation of the PPM method (without adaptivity) to solve for thickness also reduces the error by comparison with FGSH (Figure 1c), though it should be noted that since the non-PPM model setups use a diffusion based solution technique without solving separately for velocity, the impact of the PPM method is not isolated in this comparison. Both the grid adaptivity and PPM techniques provide a reduction in error for the grounded ice sheet model, and the choice of internal boundary conditions has been shown to be important when using refinement.

4. Grounding Line Migration Experiments

[41] The case of a moving grounding line is now considered in the ice stream/shelf simulations (STSF models, Table 1). In these simulations a grounding line position, calculated using the floatation criterion, is allowed to evolve during the simulation. These grounding line migration experiments are carried out on a 1000 km domain with a linearly down sloping bed from −50 m at the left boundary of the domain (ice divide) to −650 m at the right boundary (ice front). Net accumulation is uniform across the domain (see Table 2 for parameter settings).

[42] During preliminary experiments (not shown) the models are found to exhibit a region of multiple locally stable grounding line positions for a given set of inputs, within which the steady state position is sensitive to initialization. The edges of the region are robustly determined by "advance" and "retreat" experiments even when initialization is varied by changing spin-up forcing (net accumulation) and the initial thickness profile of the ice sheet. "Advance" experiments are defined such that the grounding line position moves in a seaward direction (by at least one grid cell, but typically much more) as steady state is approached, and these determine the landward edge of the region. Similarly, "retreat" experiments determine the seaward edge of the region.

[43] The steady state grounding line positions are verified through comparison against the predicted positions from the analytic solution of *Schoof* [2007] and from the moving grid MGSTXX model, which shows more self-consistent behavior than fixed grid models [*Vieli and Payne*, 2005].

[44] Equations (15) and (20) from *Schoof* [2007] give, for our setup:

$$a x_g = \left(\frac{A(\rho g)^{n+1}(1-\rho/\rho_w)^n}{4^n \beta^2} \right)^2 \left(b(x_g) \frac{\rho_w}{\rho} \right)^{n/2+2}, \qquad (16)$$

where b is the depth of the bedrock below sea level and x_g is the distance from the ice divide to the steady state grounding line position. This equation is solved numerically by finding the crossing point of the functions given by the left and right hands sides of the equation. In the current study, where b is a linear function of x, there can be only one such point, i.e., the analysis of *Schoof* [2007] predicts that there exists exactly one valid steady state grounding line position. This is at 571 km for all experiments shown. This theoretical grounding line position is shown as a dashed gray line in Figures 5, 6, and 8 (discussed in sections 4.1, 4.2, and 4.3).

[45] The uniqueness of the theoretical grounding line position implies that the steady state grounding line positions from both advance and retreat experiments should be identical, and equivalently that the region of locally stable steady state grounding line positions has length zero. The experimental design used to achieve advance and retreat experiments in the current study is now described. All the advance and retreat experiments are initialized from a slab of ice of uniform thickness H = 200 m. In the advance experiments, the models are simply spun up with a net accumulation of 0.3 m yr^{-1} to steady state. In all cases this involves advance of the grounding line as accumulation builds up on the initially thin slab of ice. The experiments shown in Figure 2 are all advance experiments.

[46] The retreat experiments involve a forcing enhancement during spin up to cause enhanced grounding line advance. This ensures that after the forcing has been reset the grounding line retreats toward its steady state. The net accumulation is initially set to the higher value of 0.5 m yr^{-1} for the first 30 kyr of the run (allowing steady state to be approached) and then reset to 0.3 m yr^{-1} (Table 2) until steady state is reached. For both retreat and advance examples see Figure 3.

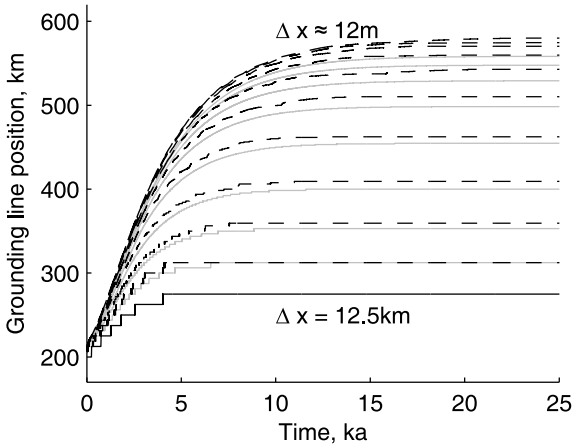

Figure 2. Time evolution of grounding line position for fixed and adaptive simulations. The solid black line shows results at resolution level 1 (Δx = 12.5 km, labeled; see also Table 3), and the gray lines show results for subsequent resolution levels up to 9 ($\Delta x \approx 49$ m) for the fixed grid FGSTSH model. The black dashed lines show results from the adaptive grid AGSTSF_GF model with maximum resolutions varying from levels 2 (Δx = 6.25 km) up to 11 ($\Delta x \approx 12$ m, labeled), base grid at resolution level 1 and $\Delta_\kappa = 2$. Steady state grounding line position increases with resolution (i.e., the higher curves in the plot are from the higher-resolution simulations).

[47] Thus, in both advance and retreat experiments a steady state is reached with identical forcing but via different paths, defining the landward and seaward limits of the region of locally stable grounding line positions. Steady states are achieved by fixed long run times, determined by visual inspection of time evolution plots and further verified as described below. This is chosen over a pure rate of change criterion due to the step like nature of grounding line position evolution (Figure 2). The advance simulations are close to steady state after 20–30 kyr, and these are terminated at 35 kyr. Similarly, the spin up phase (i.e., with the forcing enhancement) of the retreat experiments are close to steady state after 20–30 kyr. This spin up phase is terminated at 30 kyr, and a further 30 kyr of retreat after the forcing reset achieves steady state, making a total run length of 60 kyr for the retreat experiments (Figure 3). It has been established that 35 kyr and 60 kyr are sufficient to achieve steady state by verifying that the rate of change of grounding line position is less than 0.1 m yr^{-1} (it is in general much smaller than this) and by running a subset of both advance and retreat experiments to 90 kyr (not shown) to ensure that no further changes to grounding line position occur.

[48] The refinement criterion for the adaptive grid (AG) models is grounding line proximity (see section 2.2.2), with a cutoff of x_{tol} = 55 km. Since the AG models in this section all have exactly one grounding line position per refinement level at all points during their evolution, there is always exactly one patch per refinement level. The AG simulations all use a base grid at resolution level 1 (see Table 3) and a refinement factor of $\Delta_\kappa = 2$, except where stated otherwise. Every patch in every AG simulation shown corresponds to one of the resolution levels described in Table 3. Refinement frequency is 1, i.e., refinement is carried out every time step.

[49] The steady state thickness profile for a typical grounding line migration experiment, in this case model AGSTSF_GIF with a total of four refinement levels including the base grid (i.e., $\kappa = 4$), is shown in Figure 4. The higher-resolution patches are clearly shown, and in this example the steady state ice sheet is almost identical in all patches. This is not the case for the AGSTSF simulations in which each patch evolves its grounding line position inde-

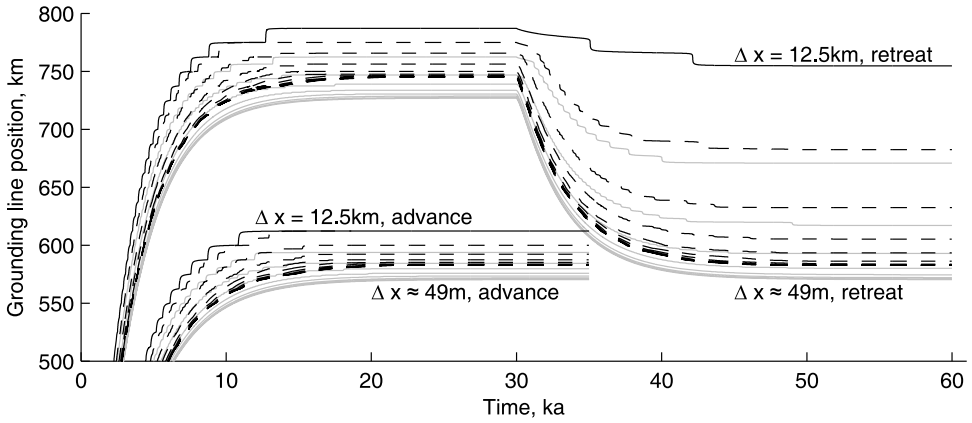

Figure 3. Time evolution of grounding line position for fixed and adaptive simulations that include the linear interpolation grounding line parameterization. The solid black lines show results at resolution level 1 (Δx = 12.5 km, see Table 3), and the gray lines show results for subsequent resolution levels up to 9 ($\Delta x \approx 49$ m) for the fixed grid FGSTSH_GI model. The FGSTSH_GI advance and retreat experiments at the highest and lowest resolutions are labeled. The dashed lines show results from the adaptive grid AGSTSF_GIF model with maximum resolution from levels 2 (Δx = 6.25 km) up to 11 ($\Delta x \approx 12$ m); base grid is held at resolution level 1 and $\Delta_\kappa = 2$. Both advance (up to 35 kyr) and retreat (up to 60 kyr) experiments are shown (section 4).

Table 3. Grid Spacing, Time Step, and Number of Grid Points Used in the Fixed Grid Models at Each Resolution Level[a]

Resolution Level	Grid Spacing, Δx	Time Step, Δt (years)	Number of Grid Points, nx
1	12.50 km	4	81
2	6.250 km	2	161
3	3.125 km	1	321
4	1.563 km	5×10^{-1}	641
5	781.3 m	2.5×10^{-1}	1281
6	390.6 m	1.25×10^{-1}	2561
7	195.3 m	6.25×10^{-2}	5121
8	97.66 m	3.125×10^{-2}	10,241
9	48.83 m	1.563×10^{-2}	20,481
10	24.41 m	7.813×10^{-3}	
11	12.21 m	3.906×10^{-3}	

[a]The first two rows are also the grid spacing and time step corresponding to the highest refinement level in adaptive grid simulations. The grid spacing and time step are halved for each increase in resolution and are shown here to four significant figures.

pendently (discussed below). A closer look at the vicinity of the grounding line (Figure 4b) shows a small discrepancy between the base grid and higher-resolution patches, probably due to truncation error.

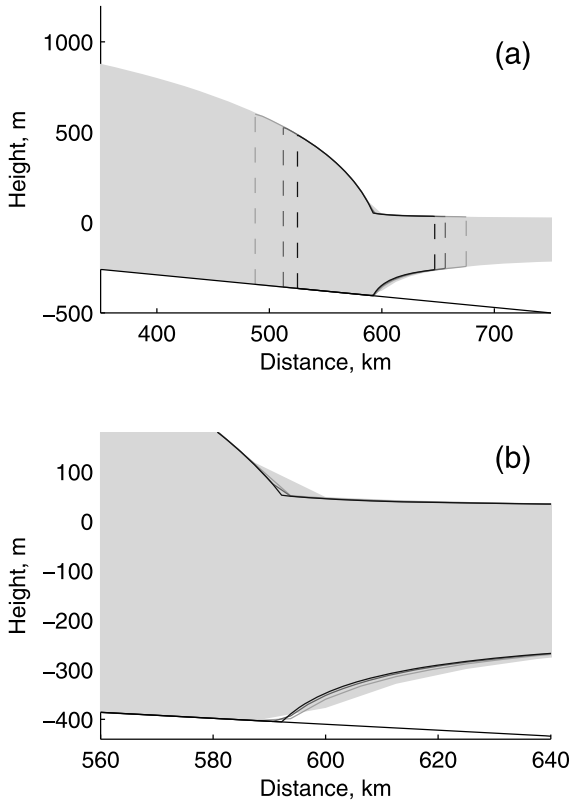

Figure 4. Steady state thickness profiles for a typical adaptive grid AGSTSF_GIF simulation for (a) just under half of the model domain and (b) at 80 km subregion in the vicinity of the grounding line. The base grid profile is shaded light gray, and higher-resolution patch profiles are depicted with solid curves (and dashed lines for lateral extents) of darker shades of gray with increasing resolution. This simulation has $\kappa_{max} = 4$ refinement levels with maximum resolution at level 4 ($\Delta x \approx 1.5$ km) (Table 3).

4.1. Fixed Grid Versus Adaptive Grid Comparison

[50] The main focus in this section will be on the simulated steady state grounding line position rather than transient behavior, as this can be verified against the analytic solution. However, we first briefly consider grounding line evolution. The transient grounding line behavior for the FGSTSF and AGSTSF_GF models is shown in Figure 2. Grounding line position advances in discrete steps, seen most clearly in the resolution level 1 ($\Delta x = 12.5$ km) simulation (black curve). This is due to the grounding line being defined as the last grounded grid point in these simulations; it must always lie on a thickness grid point. Grounding line advance is at first rapid in all experiments, as the positive accumulation thickens the ice sheet. Advance slows down as thickening and steepening of the ice sheet cause the ice discharge to come into balance with accumulation. Qualitatively, all the advance experiments share this mode of behavior.

[51] The steady state grounding line positions are now compared to the analytic solution. Figure 5 shows the dependence of steady state grounding line position on resolution for the fixed grid (FGSTSH) and adaptive grid (AGSTSH) models. Note that the resolution level (see Table 3) shown in this plot is primarily in reference to the resolution of the fixed and adaptive grid models, and does not directly relate to the grid cell size of the moving grid model (MGSTXX). This is due to the fact that the cell size in the MGSTXX model is not constant across the domain; it varies as the grid evolves. However, the average cell size in the MGSTXX model at steady state is 12.2 km at its lowest resolution, 6.6 km at the next higher resolution, etc. These values are very similar to resolution levels 1 and 2, so a direct comparison against the fixed grid cell resolution levels is still meaningful. The steady state grounding line position in MGSTXX appears to be converging with increasing resolution to a value close to the analytic solution as resolution increases (Figure 5). The MGSTXX model

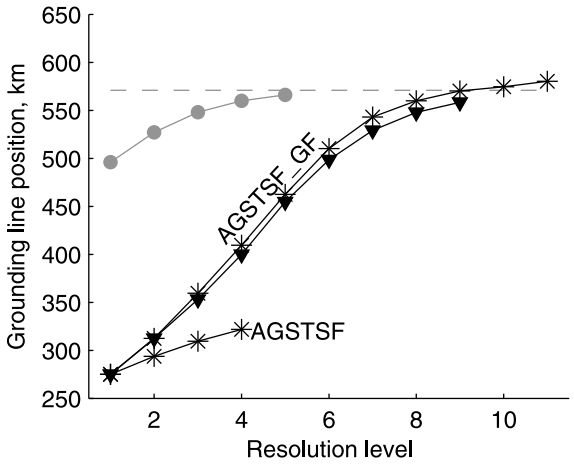

Figure 5. Convergence of steady state grounding line position with resolution levels (see Table 3) for fixed grid simulations (FGSTSF, triangles) and adaptive grid simulations (AGSTSF and AGSTSF_GF, asterisks). Only advance experiments are shown. The theoretical value (gray dashed line) and MGSTXX results (gray circles) are also shown.

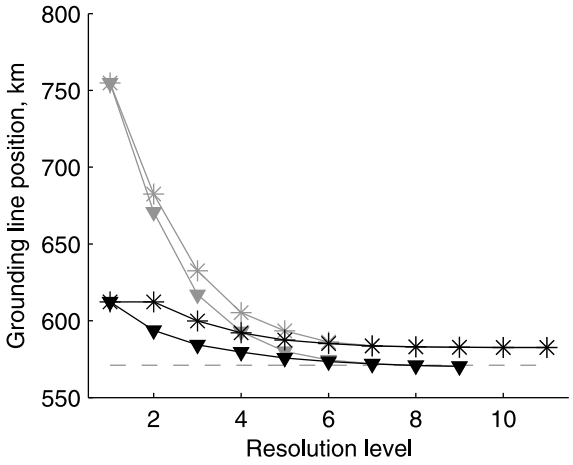

Figure 6. Convergence of steady state grounding line position with resolution levels (see Table 3) for FGSTSF_GI simulations (triangles) and AGSTSF_GIF simulations (asterisks). Results from advance experiments are shown in black, and retreat experiments are in gray. The theoretical value (gray dashed line) is also shown.

gives the same steady state grounding line position positions under both advance and retreat experiments. The FGSTSF simulations (triangles in Figure 5) appear to be starting to converge on a value close to the theoretical value, but convergence and accuracy are not fully established even at resolution level 9 (Δx = 49 m, Table 3).

[52] Steady state grounding line positions from the AGSTSF model are shown in Figure 5 (asterisks). Introducing refinement levels above the base grid does initially lead to improvements, but the steady state grounding line position appears to be converging to a position some 200–300 km short of the theoretical value. Results are not available beyond resolution level 4 due to numerical problems arising from the divergence of grounding line positions at different refinement levels. The poor performance up to level 4 is due to the base grid in the AGSTSF simulations evolving identically to the FGSTSF model run at resolution level 1, hence the patches at higher refinement levels are held back by the patch boundary conditions being consistent with a grounding line a long way short of the theoretical value. This behavior motivates the inclusion of grounding line position feedback from the highest refinement level to the base grid and all other refinement levels (AGSTSF_GIF, discussed below).

[53] It was not possible to run retreat simulations for the FGSTSF and AGSTSF models due to a numeric instability associated with grounding line retreat. The grounding line position in these models can effectively only move in steps of Δx (cell width). When the grounding line retreats by a whole grid cell in one time step, a situation can briefly arise where a very high surface slope is effectively beyond the grounding line. This implies very high gravitational driving stress with zero basal friction and can lead to very high velocities and unstable behavior. Advance experiments only are presented for models FGSTSH, AGSTSH and AGSTSH_GF.

[54] The steady state grounding line positions for the AGSTSF_GF model are shown in Figure 5. With the highest refinement level now being allowed to set the grounding line position for all lower levels (including the base grid), the AGSTSF_GF model shows remarkably similar behavior to the FGSTSF model. The adaptivity allows a higher maximum resolution to be reached, but even so convergence of steady state grounding line position with resolution cannot be established, and the value of the steady state grounding line position has advanced past the theoretical value. This model is still unstable in retreat, and the required resolution near the grounding line (level 11, $\Delta x \approx$ 12 m) is computationally demanding even with adaptivity.

4.2. Parameterizing the Grounding Line

[55] The instability in retreat of the models in the previous section, and the extremely high resolution required to get close to the analytic solution, motivates the inclusion of a parameterization for grounding line position (described in section 2.2.4). As before, we will examine the transient behavior, then compare the steady state grounding line position to the analytic solution value [*Schoof*, 2007].

[56] The time evolution of both fixed grid (FGSTSH_GI) and adaptive grid (AGSTSF_GIF) simulations incorporating linear interpolation of thickness to determine grounding line position at subgrid scale resolution are shown in Figure 3. The instability that previously arose during retreat does not occur in simulations utilizing this grounding line parameterization. Grounding line movement does not occur in discrete steps, but step-like features with magnitude Δx can still be seen. These numerical artifacts indicate that the grounding line parameterization, while allowing for the possibility of the grounding line lying at any point within its containing grid cell, does not show the same magnitude of response to the forcing at all positions within the grid cell. We speculate that there is a "preferred" grounding line location within each grid cell when using this parameterization, and grounding line migration will be slower closer to a "preferred" location than away from it. In other respects, the evolution is similar in nature to the earlier models. The retreat phase shows a similar curve to the advance phase, initially steep then leveling off to reach steady state. Retreat occurs because the accumulation is too low to balance the discharge, and slows to approach steady state when ice sheet has thinned and its slope shallowed sufficiently that accumulation and discharge can come back into balance.

[57] Steady state grounding line positions for AGSTSF_GIF and FGSTSF_GI are shown in Figure 6. Both advance and retreat experiments are shown, and both models tend to significantly over estimate the distance of the grounding line from the ice divide at lower resolutions, though this over estimation is much smaller than the under estimation seen in models AGSTSF_GF and FGSTSF (which do not include the grounding line parameterization). Approximate convergence of advance and retreat experiments with resolution is reached at around resolution level 7 ($\Delta x \approx$ 200 m) for both models. At the maximum resolution (level 11 for AGSTSF_GIF and 9 for FGSTSF_GI, see Table 3) the differences between retreat and advance steady state grounding line positions are 4 m and 37 m for AGSTSF_GIF and FGSTSF_GI, respectively. The FGSTSF_GI model converges to within 1 km of the theoretical solution. The AGSTSF_GIF model converges to 12 km above this value, possibly due to truncation errors on the base grid (discussed below).

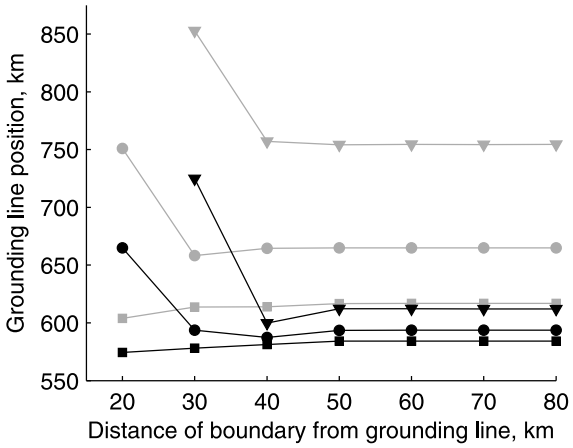

Figure 7. Impact of patch size on simulated grounding line position. Steady state grounding line positions from the AGSTSF_GIF model are shown for different values of x_{tol}, the imposed minimum distance from the grounding line to the patch boundary. Base grid resolutions (see Table 3) are 1 (triangles), 2 (circles), and 3 (squares). These correspond to Δx = 12.5 km, Δx = 6.25 km, and Δx = 3.125 km, respectively. Both advance (black) and retreat (gray) simulations are shown. The model is AGSTSF_GIF. In all cases, $\kappa_{\max}$ = 2 and Δ_κ = 1 (i.e., one patch exists in addition to the base grid and is at the same resolution as the base grid).

4.3. Sensitivity to Refinement Parameters

[58] The AGSTSF_GIF model shows convergence with resolution and reasonable accuracy O(10 km) for the implementation of refinement presented above. The refinement implementation is defined by the following refinement parameters: refinement criterion (grounding line proximity for the grounding line experiments), refinement cutoff (this is x_{tol} for the grounding line experiments), base grid resolution (Δx and Δt), refinement factor Δ_κ, and number of refinement levels $\kappa_{\max}$. Grounding line proximity is the only sensible choice of refinement criterion for the grounding line migration experiments, where our specific aim is to bring higher resolution to the vicinity of the grounding line. The adaptive versus fixed grid comparison (section 4.1) explored the impact of resolution by varying $\kappa_{\max}$. Here we investigate the robustness of the grounding line migration experiments to variations in the other three parameters, x_{tol}, base grid resolution and Δ_κ. The adaptive grid models are compared to the fixed grid models using the refinement parameters x_{tol} = 55 km, base grid resolution at level 1 (12.5 km, Table 3), and Δ_κ = 2. These three parameters are now varied one at a time, the remaining parameters keeping the standard values except where stated otherwise. The simulations shown in this section are from the AGSTSH_GIF model.

[59] Figure 7 demonstrates the impact of patch size (by varying x_{tol}). The simulations have been carried out using two refinement levels and a refinement factor Δ_κ = 1. In other words one patch exists above the base grid, and it has the same resolution as the base grid. Results are shown for resolution levels 1, 2 and 3 (Δx = 12.5 km, 6.25 km and 3.125 km, respectively; see Table 3). Experiments were carried out with x_{tol} varying from 10 km to 120 km in 10 km intervals (results for x_{tol} > 80 km not shown, but are approximately identical to x_{tol} = 80 km). Note that patch size $\geq 2 \times x_{tol}$ (can be greater than $2 \times x_{tol}$ since the patch boundaries lie at the first viable grid point at least x_{tol} from the grounding line in each direction). At all three resolutions, steady state grounding line position is independent of patch size for $x_{tol} \geq$ 50 km, but is strongly dependent for x_{tol} < 50 km. The error is large for x_{tol} < 40 km, especially at the lower resolutions. This suggests a minimum value for x_{tol} of 50 km (i.e., patch size ≥100 km) should be used for the grounding line experiments in the current study (note that x_{tol} = 55 km has been used), but this minimum patch size limit may vary with different experimental setups. It could be that the higher errors associated with smaller patch sizes arise from the inability of coarse resolution models to capture the discontinuity in thickness and velocity profiles across the grounding line.

[60] Simulations (shown in Figure 8) have been carried out using three different base grid resolutions, from level 1 (Δx = 12.5 km, see Table 3) to 3 (Δx = 3.125 km). The advance and retreat experiments converge (at or close to resolution level 8 with a tolerance of 1 km) in all cases, but the simulations with higher base grid resolution give better accuracy when compared to the theoretical grounding line position. The model-analytic solution discrepancy reduces from ≈12 km for a base grid at resolution level 1 to ≈2 km for a base grid at level 3. Thus the impact of base grid resolution on grounding line behavior in the AGSTSF_GIF model is more than an order of magnitude smaller than in the FGSTSF_GI model.

[61] The impact of refinement factor is now discussed. Figure 9 shows (black curve) the evolution of a pair of advance and retreat simulations with the standard refinement parameters and a maximum resolution at level 7 (Δx =

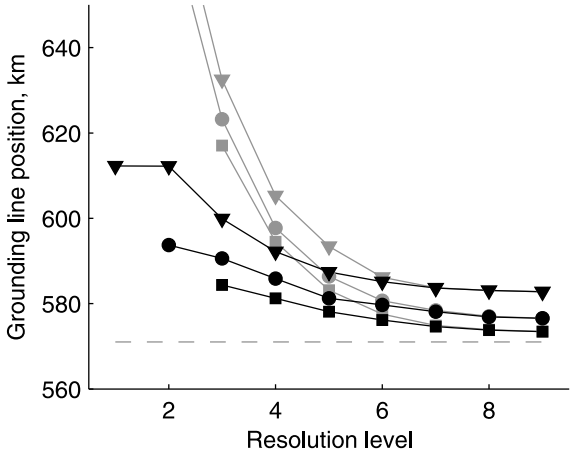

Figure 8. Impact of base grid resolution. AGSTSF_GIF steady state grounding line positions are shown against maximum resolution for simulations with base grid at resolution levels 1 (triangles), 2 (circles), and 3 (squares). These correspond to Δx = 12.5 km, Δx = 6.25 km, and Δx = 3.125 km, respectively. Advance (black) and retreat (gray) experiments are shown. The theoretical value (gray dashed line) is shown.

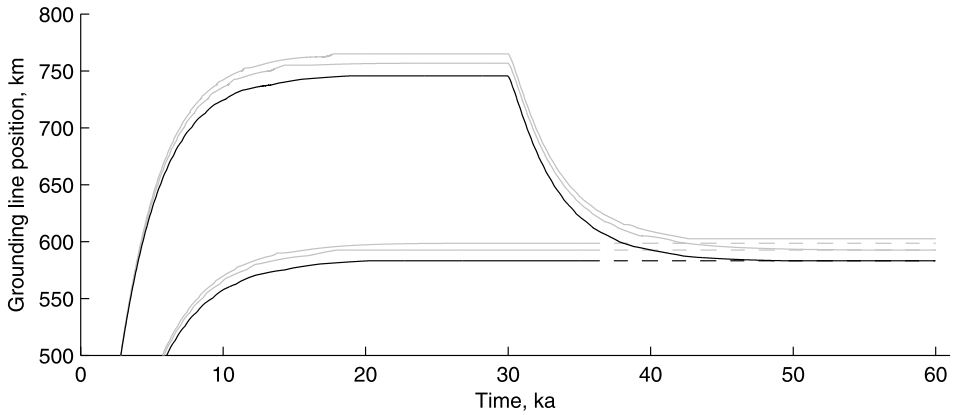

Figure 9. Impact of refinement factor. Evolution is shown for the AGSTSF_GIF model with $\Delta_\kappa = 2$ and $\kappa = 7$ (black line) and $\Delta_\kappa = 64$ and $\kappa = 2$ (gray lines). Base grid is at level 1 ($\Delta x = 12.5$ km) in all cases. Both advance (up to 35 kyr) and retreat (up to 60 kyr) simulations are shown. The steady state grounding line positions from the retreat experiments have been extended (dashed lines) to facilitate comparison between advance and retreat steady states.

195 m, Table 3). The patch size at the highest refinement level in these simulations is 91 km, slightly over $2 \times x_{tol}$. However, the patch at each lower refinement level is larger than its child, in order to provide sufficient boundary condition information (see the refinement logic in the lower part of Figure B2). This results in a patch size of 169 km at refinement level 2. Also shown in Figure 9 (in gray) are two pairs of advance/retreat simulations with a much greater jump in resolution between levels. They have $\kappa_{\max} = 2$ refinement levels, base grid resolution at level 1 ($\Delta x = 12.5$ km, see Table 3), and refinement factor $\Delta_\kappa = 64$. This gives the same maximum resolution at level 7, but in one large resolution jump instead of 6 smaller jumps. The $\kappa = 2$ patch sizes in these simulations, 150 km and 187 km, are determined by $x_{tol} = 60$ km and $x_{tol} = 70$ km respectively, chosen such that the size of the patch at refinement level 2 is comparable to that of the $\Delta_\kappa = 2$ simulations described above. This is to ensure that the internal boundaries at refinement level 2 in the simulations shown in Figure 9 are all similar (i.e., they are subjected to similar bias from the truncation errors in the base grid) so that the impacts of refinement factor can be isolated. The transient behavior of the simulations is very similar. The only difference is that the $\Delta_\kappa = 64$ simulations give slightly worse (overestimation by a further 5–10 km) steady state grounding line positions than the $\Delta_\kappa = 2$ simulation. Given this small change caused by the huge resolution jump imposed by a refinement factor of 64, we are confident that Δ_κ, does not have a large impact on the results.

[62] These experiments suggest that particular care is needed to ensure that the patch size is sufficient, and, aside from this, that refinement parameters can cause O(10 km) discrepancies in steady state grounding line position when comparing against either the theoretical position or a very high resolution fixed grid simulation. It seems likely that a significant portion of this discrepancy is due to truncation error on the base grid propagating through the patch hierarchy via the internal boundary conditions, in which case the discrepancy is dependent to some extent on the base grid resolution.

[63] To further investigate this, two additional simulations were carried out in which the grounding line was effectively held at a constant fixed position of 600 km for the duration of the simulation (i.e., β^2 was set initially for $x_g = 600$ km and was not allowed to evolve). The simulations, shown in Figure 10, were both fixed grid simulations (using model FGSTSF), and differ only in their resolution (levels 1 and 7 were used). The reason for fixing grounding line position is to isolate the truncation error from the very large errors associated with grounding line position in the low-resolution fixed grid models. It can be seen in Figure 10 that the low-resolution simulation fails to fully capture the discontinuity in thickness and velocity across the grounding line, leading to discrepancies in both terms in the floating ice, which extends right to the ice front. The lower resolution model predicts a slightly thicker, slower moving ice shelf. Reduction in this truncation error is a probable cause for the improved

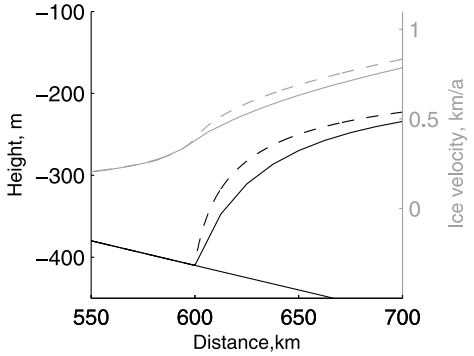

Figure 10. Near grounding line profiles in FGSTSF simulations with grounding line held fixed at 600 km from the left edge of the domain. Profiles are shown for bedrock elevation and steady state height of the ice shelf base (black) and steady state ice velocity (gray) for resolution level 1 ($\Delta x = 12.5$ km, solid lines) and resolution level 7 ($\Delta x \approx$ 195 m, dashed lines).

accuracy in the AGSTSF_GIF model when using a higher-resolution base grid (Figure 8).

5. Discussion

[64] Of the 1-D adaptive grid grounding line models presented here AGSTSF_GIF has proved most successful in the grounding line experiments. We discuss the ability of AGSTSF_GIF to provide both convergence of behavior with resolution and accuracy of steady state grounding line position, and go on to consider its applicability to modeling marine ice sheets in 2 or 3 dimensions.

5.1. Convergence Error

[65] *Vieli and Payne* [2005] showed that grounding line behavior in fixed grid models was strongly resolution dependent, and therefore not reliable for use in making predictions about the real system. In the discussion below we refer to this inconsistency relating to resolution as "convergence error." *Vieli and Payne* [2005] hypothesized that use of very high resolution could overcome resolution dependency, i.e., that a resolution threshold, Δx_t, would exist such that simulations with finer resolution than Δx_t would give consistent results. If this is true then where simulations are available with resolution above this threshold, a quantification of the convergence error in grounding line position, E_c, can be defined as the difference between a steady state grounding line prediction $x_g^{\Delta x}$ (made at resolution Δx), and the prediction x_g^c made using the very high resolution (converged) model (i.e., $x_g^c = x_g^{[\Delta x < \Delta x_t]}$),

$$E_c = |x_g^{\Delta x} - x_g^c|. \tag{17}$$

[66] Note that the convergence error is a measure of the model's self-consistency rather than an absolute error; it does not account for absolute error in the converged model prediction. Note also that advance and retreat simulations sometimes give different predicted steady state grounding line positions and hence different values for the convergence error. These can be considered as upper and lower limits for the convergence error.

[67] Our simulations (section 4.1) are not in absolute agreement with the above hypothesis. Even at very high resolution further changes in resolution cause changes in predicted grounding line position (using the above notation $x_g^{(2\Delta x)} \neq x_g^{\Delta x}$ for all Δx). However if the practical approach is taken of imposing a tolerance on x_g (of 1 km say), then we can say that the model predictions have converged by resolution level 8 ($\Delta x \approx 100$ m, see Table 3) for the FGSTSF_GI and AGSTSF_GIF models. For FGSTSF_GI, to an accuracy of 1 km,

$$x_g^c = x_g^{[\Delta x = 48.8\text{m}]} = x_g^{[\Delta x = 97.7\text{m}]} = 570\text{km}. \tag{18}$$

For AGSTSF_GIF with base grid resolution level 1 (Δx = 12.5 km), to an accuracy of 1 km,

$$x_g^c = x_g^{[\Delta x = 12.2\text{m}]} = \ldots = x_g^{[\Delta x = 97.7\text{m}]} = 583\text{km}, \tag{19}$$

where Δ_x refers to the resolution on the highest refinement level. Thus the convergence error at resolution level 3, for example, is given by

$$\begin{matrix} 14\text{km} < E_c < 47\text{km} & \text{FGSTSF\_GI} \\ 17\text{km} < E_c < 49\text{km} & \text{AGSTSF\_GIF} \end{matrix},$$

where the lower and upper limits are given by advance and retreat experiments, respectively. As this example (and the fact that both models converge at the same resolution level) shows, the convergence error is addressed with comparable success by increasing the maximum resolution in the adaptive AGSTSF_GIF model or by increasing the global resolution in the fixed grid FGSTSF_GI model. Given the increased efficiency of the AGSTSF_GIF model, this model is by far the most effective for reducing E_c.

[68] So the hypothesis of convergence of grounding line behavior with increasing resolution appears to be true, and the models shown here that include a parameterization for the grounding line position (FGSTSF_GI and AGSTSF_GIF) demonstrate convergence to within 1 km or better. *Durand et al.* [2009a, 2009b] came close to demonstrating this in their more sophisticated and computationally expensive full Stokes model, but could not run at the very high resolutions shown in the current study. The models without the grounding line parameterization (FGSTSF, AGSTSF and AGSTSF_GF) are unlikely to be adequate for making real world predictions for at least two reasons. First, they appear to be inherently unstable in retreat, hence grounding line retreat cannot, in general, be simulated. Second, the resolution required for convergence is unfeasibly high, even for adaptive models. The FGSTSF_GI model is not a candidate for full ice sheet modeling due to the requirement of grid resolution being under 100 m over the whole domain, leaving the adaptive model AGSTSF_GIF as the most promising candidate for higher-dimensional ice sheet modeling from the point of view of achieving convergence with respect to simulating grounding line motion.

5.2. Accuracy Error

[69] In addition to convergence with resolution, a requirement of the model is accuracy. The analytic steady state grounding line position [*Schoof*, 2007], which is well matched by the moving grid MGSTXX model of *Vieli and Payne* [2005], provides a reliable benchmark in terms of accuracy. We define an accuracy error, E_a, as the magnitude of the difference between our converged model predictions for steady state grounding line position and the theoretical position, x_g^t.

$$E_a = |x_g^c - x_g^t|. \tag{20}$$

We define E_a in this way such that convergence and accuracy can be considered independently from each other. So the total error, E, for any given simulation is given by the sum of convergence and accuracy errors.

$$E = E_c + E_a. \tag{21}$$

Equation (21) is not a correct representation of the difference between any given simulation and the analytic solution, due

to the possibility of errors of opposite sign canceling out. In the above definitions the two error terms cannot cancel out as we have defined them as absolute values. There are two reasons why this approach makes sense. First, if a simulation matches the analytic well because the errors happen to cancel out (e.g., the simulation falls short of the converged grounding line position and the converged grounding line position is an overestimate) then it is showing a good match for the wrong reasons and we do not wish to express confidence in this model. Second, the convergence and accuracy errors happen to be of the same sign in all the simulations discussed here, so taking their absolute values makes no difference in practice.

[70] E_a is 1 km in the fixed grid FGSTSF_GI simulations and 12 km in the adaptive grid AGSTSF_GIF simulations with base grid resolution 12.5 km (decreasing to 2 km for base grid resolution 6.25 km). This is small compared to E_c for the simulations with resolution significantly below the convergence threshold (which has been established as $\Delta \approx$ 100 m). Thus, to reduce total error the first-order term to reduce is convergence error E_c, and as discussed above, this is addressed by adaptivity far more effectively than by increasing resolution in a fixed grid model. The fact that E_a decreases with base grid resolution suggests that, consistent with model results (section 4.3 and Figure 8), E_a is mainly caused by truncation error on the base grid. It may be that the impact of this truncation error can be reduced by using different internal boundary conditions, and this is a planned future development.

[71] Since the total error in any adaptive simulation is the sum of convergence and accuracy errors, in order to optimize the benefit of adaptivity these two sources of error should be of the same order of magnitude. In practice this means that appropriate selection of base grid resolution and maximum resolution will be an important factor in getting the most benefit from adaptive mesh refinement. For example, in the AGSTSF_GIF model base grid at resolution level 3 ($\Delta x \approx 3$ km) and maximum resolution at level 6 ($\Delta x \approx 0.4$ km) gives $E_c = 2$ km, $E_a = 2$ km and hence total error $E = 4$ km. This allows the user a level of control over use of computational resource that cannot be exercised in fixed grid models.

5.3. Computational Efficiency

[72] The above discussion highlights the importance of the main advantage of adaptivity over fixed grid models: computational efficiency. As a crude indication of the computational gain, the AGSTSF_GIF model can simulate two resolution levels higher (i.e., Δx a factor 4 smaller, see Table 3) than the FGSTSF_GI model, at a comparable computational cost. For example the FGSTSF_GI simulations at resolution level 8 and the AGSTSF_GIF simulations with base grid at level 1 and maximum resolution at level 10 (a factor 4 higher resolution than level 8) all took O(100 h). This is with refinement occurring on every time step, without optimizing the code, and with a refinement factor $\Delta_\kappa = 2$, all of which could probably be improved upon in terms of computational efficiency. In particular, a higher refinement factor will reduce the number of calculations that need to be made (in fact CHOMBO is typically used with refinement factor $\Delta_\kappa = 4$ [*Meglicki et al.*, 2007]). The benefits of adaptivity are potentially greater with more dimensions than one, especially so if only the grounding lines of marine ice sheets require higher resolution within simulation of the whole Antarctic ice sheet. With these factors in mind, we would anticipate being able to resolve the grounding line with an order of magnitude increase in resolution in a two- or three-dimensional model by using adaptivity (as compared to a fixed grid model with the same computational cost).

5.4. Transient Response

[73] The main focus of the analyses and discussion in the current study is steady state grounding line behavior. However, in order to be used in model-based future change predictions the rate of change of grounding line position also needs to be assessed. Whilst such an analysis is beyond the scope of the current study it is worth pointing out that the time-dependent behavior of the grounding line does converge with resolution in much the same way as the steady state behavior (Figures 2 and 3), for both fixed and adaptive grids. Future studies within the "Marine Ice Sheet Model Intercomparison Project" (MISMIP) will incorporate analyses of time-dependent behavior across a range of different models. Given that the analytic solution of *Schoof* [2007] used to verify steady state grounding line positions does not predict time-dependent grounding line behavior, an intercomparison of many different models (MISMIP in this case) provides a better setup for assessment of transient behavior.

5.5. Higher-Dimension Ice Sheet Models

[74] When implementing whole ice sheet simulations in more than one-dimensional refinement is likely to be of use not only for grounding line migration but also for simulating ice streams, in which case estimated truncation error (which has been shown to be effective in the grounded ice sheet studies of section 3) is likely to be a better refinement criterion. In this case the truncation error refinement criterion and the grounding line proximity refinement criterion can be used in the same simulation, with grid cells that qualify by either criterion being marked for refinement. Adaptive mesh refinement will be a powerful tool for such simulations, but as shown in section 4.3 the refinement parameters must be chosen with care, and probably accompanied by sensitivity analyses. Choice of refinement criteria and their corresponding cutoffs (e.g., x_{tol}, estimated truncation error), refinement frequency, base grid resolution, Δ_κ and κ all offer the user control over how computational resource is used, and all have the potential to influence the model output.

6. Conclusions

[75] We have demonstrated that a specialized numerical scheme designed to solve hyperbolic-type equations, the piecewise parabolic method (PPM), can be successfully applied to 1-D ice sheet models, and intend to trial this scheme in higher dimensions in the future. The results presented here support the conclusion of *Vieli and Payne* [2005] that standard fixed grid models exhibit grounding line behavior that is highly resolution dependent when run at easily achievable resolutions, and also their speculation that

these problems could be overcome at very high resolution. We have shown that such high resolution can be achieved more effectively through use of AMR than with a fixed grid model.

[76] We have shown that conventional fixed grid models are potentially unstable when used for grounding line retreat experiments, and are also inaccurate (except possibly at unfeasibly high resolution). Use of standard AMR does not resolve any of these issues, but implementing grounding line position feedback within AMR does improve accuracy and reduces resolution dependence.

[77] Parameterization of grounding line position based on the floatation condition (similar but not identical to *Pattyn et al.* [2006]) in a standard fixed grid model provides an improvement and solves the instability issue. However, very high resolution (O(100 m) or better) must be achieved in order to give accurate and resolution independent results. This is not currently achievable in full ice sheet models for Antarctica or Greenland.

[78] AMR, used with both linear interpolation based on the floatation condition at the highest refinement level and feedback of grounding line position to all lower refinement levels, also provides good results, but at a more achievable computational cost. Very small patches (that is with boundaries within 50 km of the grounding line in the current study, though this may vary) should be avoided during grid refinement. AMR allows the modeler to balance the convergence and accuracy errors (E_c and E_a, defined in section 5), thus reducing the total error, through choice of refinement parameters such as base grid and maximum resolutions. The current setup suggests that a base grid resolution of O(1 km) and a maximum resolution O(100 m) would provide accurate and self consistent steady state grounding line predictions. This is likely to vary depending on experimental setup, and it might be possible to improve on this (i.e., relax the resolution requirements) with future developments (for example improved parameterizations for the grounding line, also internal boundary conditions or multigrid techniques that reduce the impact of base grid truncation error).

[79] These conclusions are based on verification against moving grid models, analytic solutions, and remain to be validated against real world data. There is no reason to suspect that the improvements attributable to introducing AMR in 1 dimension will not also be manifest in higher dimensional models. Indeed, we would expect the efficiency gain to be greater in large-scale ice sheet models since the proportion of the domain very close to the grounding line will likely be smaller with 2 spatial dimensions than with 1. The use of AMR, grounding line parameterization and PPM shows promise for use in large-scale ice sheet modeling. We anticipate that a 3-D AMR ice sheet model of the whole of Antarctica is achievable, making use of third party software (e.g., CHOMBO [*Meglicki et al.*, 2007]) to implement the adaptivity in an existing fixed grid ice sheet model (e.g., GLIMMER [*Rutt et al.*, 2009], which now includes a higher-order ice dynamical solver). This model would have grounding line migration capability and also the ability to direct the adaptivity to particular features or regions of interest, such as fast flow features or the Pine Island Glacier catchment. This would constitute a significant step forward in our ability to make predictions about the future behavior of marine ice sheets and their impact on global sea level.

Appendix A: Thickness Evolution—The Piecewise Parabolic Method

A1. Introduction

[80] The piecewise-parabolic method (PPM) was developed by *Colella and Woodward* [1984] to simulate strong shocks and discontinuities in gases. The PPM scheme is not limited to astrophysics and engineering applications; it has been successfully used in other fields such as meteorology [*Lin and Rood*, 1996; *Carpenter et al.*, 1990] and oceanography [*James*, 1996]. Given the PPM's diverse background, it seems a good candidate to be used as a thickness solver in an ice sheet model.

[81] The advantages of the PPM to ice dynamics, in particular, include its ability to preserve surface shapes, to handle abrupt changes in direction, to represent steep gradients such as at the ice margins and to handle nonuniform grid spacing. The PPM scheme is still diffusive but much less so than other lower-order schemes. We anticipate that the scheme can capture abrupt changes in direction between flow features such as at the lateral boundaries of ice streams and at the grounding line. Nonuniform grid spacing means that a grid with high resolution in areas of steep gradients, such as at ice margins, and with low resolution in areas of uniform flow, such as the interior of an ice sheet, can be used, complementing adaptivity (Appendix B). The PPM scheme was not only designed to calculate fluxes but to solve the coupled system of equations for mass, momentum and energy. This feature offers no real benefit to ice dynamics because the momentum equation for ice flow is elliptical rather than hyperbolic and so is best solved using a separate scheme.

[82] The PPM scheme is explained in general terms below and its implementation to an ice flow model is explained in section 2. We use a modified version of the code, VH-1, written by the Numerical Astrophysics Group at the University of Virginia Institute of Theoretical Astrophysics in 1990–1991.

A2. PPM Interpolation Scheme

[83] In this section *Colella and Woodward* [1984, hereafter C&W] piecewise-parabolic interpolation is described for variable H whose behavior is determined by a 1-D hyperbolic equation in x. The computational domain is divided into N zones, i.e., intervals whose widths may differ. The discrete value of H corresponding to each zone is the average of the continuous variable across the interval. Let $x_{j+\frac{1}{2}}$ be the boundary between the jth and $(j + 1)$ th zones and assume that the average value of H between $x_{j-\frac{1}{2}}$ and $x_{j+\frac{1}{2}}$ at time t^k is

$$H_j^k = \frac{1}{\Delta x_j} \int_{x_{j-\frac{1}{2}}}^{x_{j+\frac{1}{2}}} H\left(x, t^k\right) dx, \tag{A1}$$

where $\Delta x_j = x_{j+\frac{1}{2}} - x_{j-\frac{1}{2}}$.

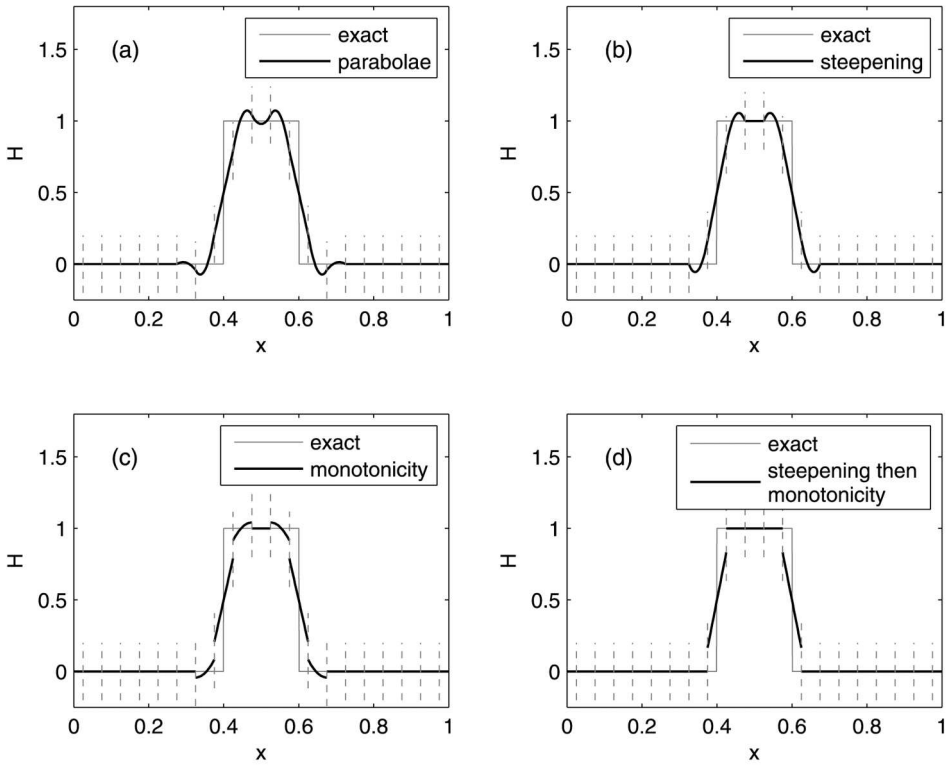

Figure A1. PPM representation of a rectangular wave distribution. The domain is divided into 21 zones (vertical dashed lines mark the zone edges), and discrete values of the wave distribution (gray solid line) at the center of the zones are passed to the PPM scheme. Various stages of construction of the interpolation function (solid black line) are shown: (a) the initial parabolic interpolation, (b) steepening of the interpolated function, (c) monotonicity constraint applied to the interpolated function, and (d) the complete function.

A2.1. Spatial Interpolation

[84] A piecewise continuous interpolation function, f^H, is constructed such that its average value across jth zone is equal to the known average H_j^k and is constrained such that local extrema in the interpolation function are removed. The PPM scheme assumes that spatial distribution of H has a parabolic profile in each zone given by

$$H(x) = H_{L,j} + \zeta\left(\Delta H_j + H_{6,j}(1-\zeta)\right), \tag{A2}$$

where

$$\zeta = \frac{x - x_{j-\frac{1}{2}}}{\Delta x_j}, \qquad x_{j-\frac{1}{2}} \le x \le x_{j+\frac{1}{2}}. \tag{A3}$$

The coefficients of the parabola, ΔH_j and $H_{6,j}$, are given by

$$\begin{aligned} \Delta H_j &= H_{R,j} - H_{L,j}, \\ H_{6,j} &= 6\left(H_j^k - \frac{1}{2}\left(H_{L,j} + H_{R,j}\right)\right), \end{aligned} \tag{A4}$$

where $H_{L,j}$ and $H_{R,j}$ are the limits of parabolic distribution at the left and right edges of the jth zone, respectively. The construction of these is depicted in Figure A1 and described below.

[85] An approximation of $H_{j+\frac{1}{2}}$, the value of H at the zone edge $x_{j+\frac{1}{2}}$, is obtained using interpolation across 4 zones, two either side of the zone edge (see Figure A1a). Details of the scheme are given by C&W and will not be repeated here. The formula for $H_{j+\frac{1}{2}}$ is given by equation (1.6) of C&W with the average slope replaced by the modified value given by expression 1.8 of C&W.

[86] The slope is steepened at a discontinuity in H and modified such that the value of $H_{j+\frac{1}{2}}$ always lies between H_j and H_{j+1}. Both the values of $H_{L,j+1}$ and $H_{R,j}$ are set to $H_{j+\frac{1}{2}}$ and using these values, the coefficients of the parabola given by expression (A4) are then calculated. At this stage the parabolic profiles produce a continuous function representing H (Figure A1b).

[87] Each zone is then checked in turn to see if the interpolation function takes values outside $H_{L,j}$ and $H_{R,j}$ and if it does a monotonicity constraint is applied through expressions 1.10 of C&W (Figure A1c). This means that if H_j^k is a local maximum then $H(x)$ is set to a constant, i.e., $H_{L,j}$ and $H_{R,j}$ are reset to H_j^k. If the function overshoots, i.e., the coefficients of the parabola do not satisfy $|\Delta H_j| \ge |H_{6,j}|$, then either $H_{L,j}$ or $H_{R,j}$ is reset so that $H(x)$ is a monotonic function across each zone.

[88] The coefficients of the parabolic profiles are recalculated. The resulting interpolation function represent-

ing H may be discontinuous at the zone edges, as shown in Figure A1d.

A2.2. Advecting Forward in Time

[89] The PPM scheme implements advection of H by calculating fluxes across zone boundaries. This is done by first calculating $\overline{H}$, the temporal mean of H, at the zone boundary over the duration of a forward time step.

[90] It is assumed that the behavior of the hyperbolic equation describing H for one time step can be approximated by the linear first-order wave equation. This means that the spatial distribution created by the parabolic profiles given by equation (A2) at time t^k does not change as it is advected with velocity u through time step Δt, i.e., $H(x, t^k + \Delta t) = H(x - u\Delta t, t_k)$ where Δt satisfies the stability condition $u\Delta t \leq \min_j \Delta x_j$. It follows that the temporal average of H at a given point can be found by simply taking a spatial average of the interpolation function over a distance $|u\Delta t|$ to the left (right) of the point if the velocity is positive (negative).

[91] Let averages of the interpolation function f^H to the left and right of the zone edge $x_{j+\frac{1}{2}}$ be defined by

$$\begin{aligned} f^H_{j+\frac{1}{2},L}(\eta) &= \tfrac{1}{\eta}\int_{x_{j+\frac{1}{2}}-\eta}^{x_{j+\frac{1}{2}}} H(x)dx \\ f^H_{j+\frac{1}{2},R}(\eta) &= \tfrac{1}{\eta}\int_{x_{j+\frac{1}{2}}}^{x_{j+\frac{1}{2}}+\eta} H(x)dx \end{aligned}, \tag{A5}$$

where η is the distance from the zone edge over which the averages are taken. Performing the integration on the parabolic profiles given by equation (A2) with the calculated values for $H_{L,j}$ and $H_{R,j}$ the averages can be written as

$$f^H_{j+\frac{1}{2},L}(\eta) = H_{R,j} - \frac{\eta}{2\Delta x_j}\left(\Delta H_j - \left(1 - \frac{2}{3}\frac{\eta}{\Delta x_j}\right)H_{6,j}\right), \tag{A6}$$

$$f^H_{j+\frac{1}{2},R}(\eta) = H_{L,j+1} - \frac{\eta}{2\Delta x_{j+1}}\left(\Delta H_{j+1} + \left(1 - \frac{2}{3}\frac{\eta}{\Delta x_{j+1}}\right)H_{6,j+1}\right). \tag{A7}$$

[92] By taking the upwind average of the interpolation function, the temporal average of H at the zone edge $x_{j+\frac{1}{2}}$ is obtained

$$\overline{H}_{j+\frac{1}{2}} = \begin{cases} f^H_{j+\frac{1}{2},L}(u\Delta t) & \text{if } u \geq 0 \\ f^H_{j+\frac{1}{2},R}(-u\Delta t) & \text{otherwise.} \end{cases} \tag{A8}$$

This value of $\overline{H}_{j+\frac{1}{2}}$ is used to calculate the flux of H from the jth to the $(j+1)$ th zones. The resulting fluxes can be differenced conservatively and are at least third-order accurate in space and time, increasing to 4th order when the zones are equally spaced and the time step tends to zero.

A2.3. Boundary Conditions

[93] The boundary conditions are applied through ghost zones, i.e., zones lying outside the physical domain, to preserve the stencil of the PPM scheme. H in six ghost zones, three at each end of the computational domain, are required to calculate the flux through the outer edges of the physical domain. This breaks down as follows: The interpolation function averages $f^H_{\frac{1}{2},L}$ ($f^H_{N+\frac{1}{2},R}$) at the left (right) hand boundary use interpolated H across one ghost zone adjacent to the boundary. To construct the parabolae for the interpolation, values for H in an additional two ghost zones are required.

[94] The values of H and the widths of the ghost zones are specified at the start of each H calculation and depend on the boundary conditions of the problem. Good choices will lead to a parabolic function inside the physical domain. The specific boundary condition implementations used in the ice sheet models used in the current study are described in section 2.2.3.

Appendix B: Adaptive Mesh Refinement

[95] Structured Adaptive Mesh Refinement (SAMR or more generally AMR) allows a computer model to introduce new higher-resolution subregions within a domain as the model state evolves forward through time [*Berger and Oliger*, 1984]. This technique is most beneficial in problems where small subregions of the model domain require much higher resolution than the rest of the domain in order to provide a sufficiently accurate solution. This is the case, for example, in cosmological simulations [*Vazza et al.*, 2009; *Skillman et al.*, 2008]. This is certainly also true of ice sheets, which typically have narrow (compared to the whole ice sheet), fast flowing outlet glaciers known as ice streams. The fine horizontal scale of ice stream motion compared to the more uniform slow flow of the ice sheet interior, and in particular the narrow deformation zones at the ice stream edges, indicate the need for a finer resolution in their part of the model domain in order to adequately resolve such features. The focus in this study will be on bringing higher resolution to within a few tens of kilometers of the grounding line to assess whether this allows for a more accurate simulation of grounding line motion. The portion of the model domain containing the grounding line is a small fraction of the ice sheet as a whole, and so the problem is well suited to AMR.

[96] In two or more dimensions AMR can be quite intricate, and third party libraries have been written to provide parallelized AMR implementations [*MacNeice et al.*, 2000; *Hornung and Kohn*, 2002; *Meglicki et al.*, 2007]. In the current study results are presented from experiments conducted using a stand-alone code written by the authors to provide AMR in a 1-D ice sheet model.

B1. Overview and Terminology

[97] The two key phases of an AMR simulation are model evolution and grid refinement. The model evolves forward in time for a prescribed number of time steps, after which refinement of the grid takes place, potentially leading to a new set of nested grids. These two phases are then repeated until the end of the run.

[98] During the evolution phase, the base grid and each patch evolve as would a non-AMR model, with one or two exceptions (discussed below, after the terminology is introduced). The grid refinement process is at the core of AMR and is described fully in section B2.

[99] The following terminology is required in order to fully describe the adaptivity.

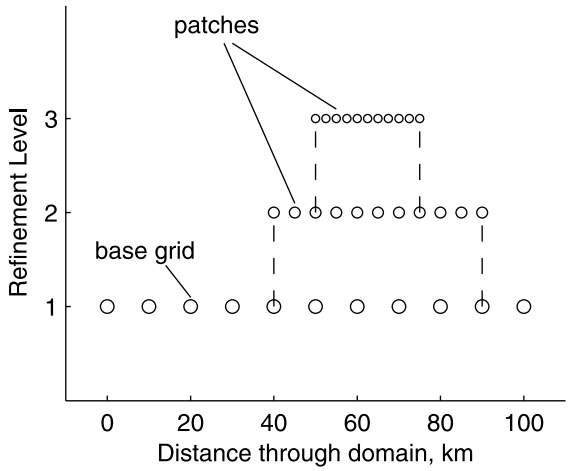

Figure B1. Example of patch hierarchy with three refinement levels (including the base grid). The circles indicate the active grid points (solution will only be calculated on active points). The base grid is always active over the entire model domain. The black dashed lines highlight the spatial relationship between refinement levels: each patch is spatially contained within a parent patch (or the base grid) at one lower refinement level. For clarity, the staggered grid is not shown here.

[100] 1. Mesh (or grid): A discretization of the model domain (used interchangeably).

[101] 2. Base grid: A grid covering the whole model domain at the lowest resolution for a given simulation.

[102] 3. Patch: A contiguous region of grid cells and their data at a given resolution, spanning a subregion of the model domain.

[103] 4. Patch hierarchy (or grid hierarchy): Hierarchical grid structure over all refinement levels, see Figure B1. This defines the extent of all the patches at any point during the simulation.

[104] 5. Refinement level κ, of a patch: The number of increases in resolution from the base grid. Note that this is inclusive of the base grid (e.g., $\kappa = 1$ refers to the base grid and a patch 2 refinement levels above the base grid would be at level $\kappa = 3$).

[105] 6. Higher/lower: By convention, moving "upward" or "higher" through the patch hierarchy means moving to higher resolution, and moving "downward" or "lower" means moving to a lower resolution.

[106] 7. Refinement factor, Δ_κ: The ratio of cell size at a given resolution to cell size at the next higher resolution. In the current study Δ_κ will be held constant for any given simulation, though this need not be the case in general.

[107] 8. Maximum number of levels, $\kappa_{\max}$, of a simulation: the maximum number of allowable refinement levels, imposed to prevent the resolution from becoming too high to handle computationally.

[108] 9. Refinement: The process of marking grid points that need higher resolution, and creating a new patch hierarchy. This is based on the refinement criterion.

[109] 10. Refinement criterion: A measure that can be calculated in order to determine which grid cells need to be run at a higher resolution.

[110] 11. Refinement interval, n_r: An integer set by the user. Grid refinement is applied once every n_r time steps of evolution on the base grid.

[111] 12. Internal boundary: The boundary of a patch where it does not coincide with a boundary of the base grid.

[112] 13. Parent: A parent of a patch is a patch at the next lower refinement level (i.e., coarser resolution) that spatially encompasses the patch.

[113] 14. Child: A child of a patch is a patch at the next higher refinement level (i.e., finer resolution) that is spatially contained within the patch.

[114] To put this terminology into context: at any point during an AMR simulation the entire domain is being evolved at low resolution on the base grid, which spans the entire model domain. A number of patches at higher resolutions ($\kappa > 1$) might exist, on which subregions of the domain are being evolved at higher resolutions. The patches (described at any point in time by the patch hierarchy) might expand or shrink, appear or vanish, at any time during the simulation, depending on the evolution of the solution and on the refinement criterion.

[115] The spatial resolution at any given refinement level κ is given by

$$\Delta x_\kappa = \frac{\Delta x}{\Delta_\kappa^{(\kappa-1)}}, \tag{B1}$$

where Δx is the spatial resolution on the base grid. Hence the maximum resolution allowable in a given simulation is $\Delta_\kappa^{(\kappa_{\max}-1)} \times \Delta x$. Temporal resolution is also determined by the refinement factor Δ_κ. The current study calculates the time step at each refinement level in the same way as the grid size (substitute Δt for Δx) in equation (B1), consistent with the CFL condition [*Courant et al.*, 1928].

[116] It should be emphasized that the flow of information through the patch hierarchy is in general one way: upward. Patches at higher refinement levels (i.e., higher resolution) have no influence on patches at lower refinement levels (i.e., lower resolution). This means that the region covered by a patch at the third refinement level (for example) is being simulated at three (or more) different resolutions, of which only the highest will contribute to the final output. There are two exceptions to this upward information flow:

[117] For certain types of internal boundary conditions, it is possible for higher levels to influence the size of their parent patches (see section 2.2.3.4). For some of the grounding line migration experiments, the grounding line position is passed back down through the patch hierarchy (see section 2.2.2).

B2. Refinement

[118] An initial grid hierarchy is defined at the start of a model run, and periodically refined (once every n_r time steps) during the run. The maximum number of refinement levels is defined by the user at the start of a simulation. Refinement can be summarized in three steps, which are explained in more detail in the rest of this section:

[119] 1. Use a prescribed refinement criterion to mark grid points for running at higher resolution (see section 2.2.1 or 2.2.2).

[120] 2. Decision making logic to create new patches (Figure B2).

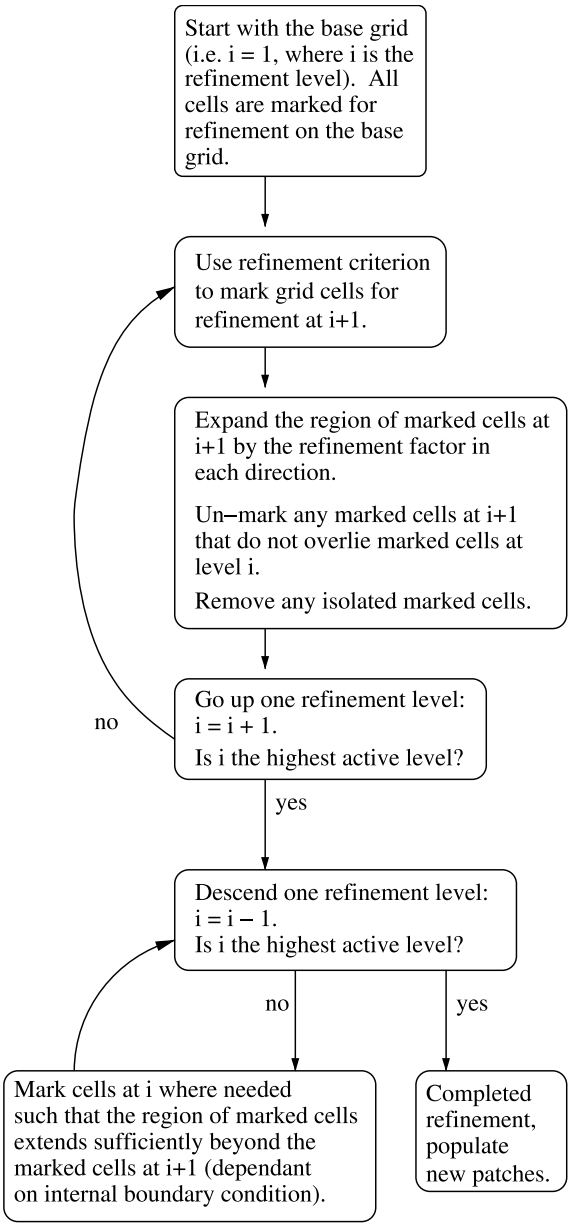

Figure B2. Flow diagram showing steps taken during the grid refinement process. See Appendix B for a description of the terminology used.

[121] 3. Initialize patches using data from parent patches (section 2.2.3).

[122] The two different types of refinement criterion used in the current study are Richardson truncation error estimation (section 2.2.1) and grounding line proximity (section 2.2.2).

[123] Figure B2 shows the decision logic that surrounds the refinement criterion and results in establishing a new patch hierarchy. Most of the work (including the calculation of the refinement criterion) is done in the ascending loop (from base grid to highest refinement level), but a descending loop is also present (seen in the lower part of Figure B2). The latter is simply to ensure that sufficient data are available to provide internal boundary conditions at each level, and is only carried out for certain types of internal boundary condition.

B2.1. Refinement Using Truncation Error

[124] The Richardson truncation error is estimated on any given patch by running the model for two time steps at two times higher resolution than normal and using the method of *Berger and Oliger* [1984]:

$$\frac{Q^2u(x,t) - Q_{2h}u(x,t)}{2^{q+1}-2} = \tau + O\left(h^{q+2}\right), \tag{B2}$$

where Q is the difference operator (so Q^2 represents two forward time steps), q is the expected order of accuracy, u is the variable for which we are solving (velocity in our case) as a function of distance, x, and time, t, and τ is the estimated truncation error of u. Q_{2h} is the difference operator run at a factor of two lower resolution (both spatially and temporally) compared to Q.

[125] We define a cutoff value τ_c at the start of each run. During grid refinement we implement the following procedure for each patch (including the base grid) in order to determine which cells satisfy the refinement criterion:

[126] 1. Create a new child patch covering the same region as its parent but with double the resolution, initialize it from the parent patch using stored values from the previous time step, and run it forward for two time steps (time steps being half the length of those for the parent).

[127] 2. We use the latest values for the patch and the new child patch to calculate the Richardson truncation error τ.

[128] 3. Mark all grid points for refinement for which $\tau > \tau_c$. This corresponds to the second bubble in Figure B2.

B2.2. Refinement by Grounding Line Proximity

[129] For grounding line migration experiments, the aim of refinement is to bring higher resolution to the immediate vicinity of the grounding line. This is implemented by marking for refinement all cells within a certain distance, x_{tol}, of our estimates for the grounding line position, x_g. The refinement criterion for refinement level κ in distance from edge of domain, x, is given by

$$\min\left(x_g^*, x_g(\kappa)\right) - x_{tol} < x < \max\left(x_g^*, x_g(\kappa)\right) + x_{tol}, \tag{B3}$$

where $x_g(\kappa)$ is the grounding line position at refinement level κ and x_g^* is our "best" estimate for grounding line position. We assume that the "best" estimate for grounding line location is given at the highest active refinement level, $\kappa_{\max}$, i.e., $x_g^* = x_g(\kappa_{\max})$. All grid points that satisfy equation (B3) (i.e., values of x that lie exactly on grid points and satisfy equation (B3)) are marked for refinement. This corresponds to the second bubble in Figure B2.

[130] For some simulations (section 2.2.4.1) the grounding line position at the highest level is passed back to all patches. In this case the refinement criterion equation (B3) simplifies to

$$x_g^* - x_{tol} < x < x_g^* + x_{tol}. \tag{B4}$$

In practice, x_{tol} can also be defined by (a combination of distance and) number of grid cells (e.g., $x_{tol} = 10 \times \Delta x$ where Δx is grid cell slze), providing successively smaller

grounding line vicinity patches for successively higher refinement levels.

B2.3. Patch Initialization

[131] Once the patch hierarchy has been created, the next step is to populate it with appropriate data values. This corresponds to the final (bottom right) bubble in Figure B2. Entirely new patches are populated using linear interpolation from parent patches. Where the new patch hierarchy contains patches that were partially in existence prior to grid refinement, only new grid points that were not previously contained in a patch are populated (again by linear interpolation), otherwise cells keep their values from the previous time step.

[132] Boundary condition data at the edge of patches are usually provided by parent patches (section 2.2.3.4). In the case of the base grid, or boundaries of patches that overlie the edge of the base grid, the appropriate global boundary condition is used (sections 2.1.3 and 2.2.3.1).

[133] **Acknowledgments.** The authors would like to thank Frank Pattyn, Stephen Price, and one anonymous reviewer for their useful criticisms that have improved the quality of the paper. This work was supported by the United Kingdom's National Centre for Earth Observation cryosphere and climate themes as well as the project "Understanding contemporary change in the West Antarctic ice sheet" funded by NERC standard grants NE/E006256/1 and NE/E006108/1.

References

Berger, M. J., and J. Oliger (1984), Adaptive mesh refinement for hyperbolic partial differential equations, *J. Comput. Phys.*, *53*, 484–512, doi:10.1016/0021-9991(84)90073-1.

Carpenter, R. L., Jr., K. K. Droegemeier, P. R. Woodward, and C. E. Hane (1990), Application of the piecewise parabolic method (PPM) to meteorological modelling, *Mon. Weather Rev.*, *118*(3), 586–612, doi:10.1175/1520-0493(1990)118<0586:AOTPPM>2.0.CO;2.

Colella, P., and P. R. Woodward (1984), The piecewise parabolic method (PPM) for gas-dynamical simulations, *J. Comput. Phys.*, *54*, 174–201, doi:10.1016/0021-9991(84)90143-8.

Courant, R., K. Friedrichs, and H. Lewy (1928), "ber die partiellen differenzengleichungen der mathematischen physik", *Math. Ann.*, *100*(1), 32–74, doi:10.1007/BF01448839.

Durand, G., O. Gagliardini, B. de Fleurian, T. Zwinger, and E. le Meur (2009a), Marine ice sheet dynamics: Hysteresis and neutral equilibrium, *J. Geophys. Res.*, *114*, F03009, doi:10.1029/2008JF001170.

Durand, G., O. Gagliardini, T. Zwinger, E. le Meur, and R. C. A. Hindmarsh (2009b), Full Stokes modelling of marine ice sheets: Influence of the grid size, *Ann. Glaciol.*, *50*, 109–114, doi:10.3189/172756409789624283.

Goldberg, D., D. M. Holland, and C. Schoof (2009), Grounding line movement and ice shelf buttressing in marine ice sheets, *J. Geophys. Res.*, *114*, F04026, doi:10.1029/2008JF001227.

Hindmarsh, R. C. A., and A. J. Payne (1996), Time step limits for stable solutions of the ice-sheet equation, *Ann. Glaciol.*, *23*, 74–85.

Hornung, R. D., and S. R. Kohn (2002), Managing application complexity in the SAMRAI object-oriented framework, *Concurrency Comput. Pract. Exp.*, *14*(5), 347–368, doi:10.1002/cpe.652.

Hutter, K. (1983), *Theoretical Glaciology Material Science of Ice and the Mechanics of Glaciers and Ice Sheets*, D. Reidel, Dordrecht, Netherlands.

James, I. D. (1996), Advection schemes for shelf sea models, *J. Mar. Syst.*, *8*, 237–254, doi:10.1016/0924-7963(96)00008-5.

Katz, R. F., and M. G. Worster (2010), Stability of ice-sheet grounding lines, *Proc. R. Soc. A*, *466*, 1597–1620, doi:10.1098/rspa.2009.0434.

Lin, S. J., and R. B. Rood (1996), Multidimensional flux-form semi-Lagrangian transport schemes, *Mon. Weather Rev.*, *124*(9), 2046–2070, doi:10.1175/1520-0493(1996)124<2046:MFFSLT>2.0.CO;2.

MacNeice, P., et al. (2000), PARAMESH: A parallel adaptive mesh refinement community toolkit, *Comput. Phys. Commun.*, *126*, 330–354, doi:10.1016/S0010-4655(99)00501-9.

Meglicki, Z., S. K. Gray, and B. Norris (2007), Multigrid FDTD with Chombo, *Comput. Phys. Commun.*, *176*, 109–120, doi:10.1016/j.cpc.2006.08.008.

Mercer, J. H. (1978), West Antarctic ice sheet and CO_2 greenhouse effect-threat of disaster, *Nature*, *271*, 321–325, doi:10.1038/271321a0.

Paterson, W. S. B. (1994), *The Physics of Glaciers*, 3rd ed., Elsevier, New York.

Pattyn, F., A. Huyghe, S. Brabander, and B. De Smedt (2006), Role of transition zones in marine ice sheet dynamics, *J. Geophys. Res.*, *111*, F02004, doi:10.1029/2005JF000394.

Pollard, D., and R. M. DeConto (2009), Modelling West Antarctic ice sheet growth and collapse through the past five million years, *Nature*, *458*, 329–332, doi:10.1038/nature07809.

Rutt, I. C., M. Hagdorn, N. R. J. Hulton, and A. J. Payne (2009), The Glimmer community ice sheet model, *J. Geophys. Res.*, *114*, F02004, doi:10.1029/2008JF001015.

Schoof, C. (2007), Ice sheet grounding line dynamics: Steady states, stability and hysteresis, *J. Geophys. Res.*, *112*, F03S28, doi:10.1029/2006JF000664.

Skillman, S. W., B. W. O'Shea, E. J. Hallman, J. O. Burns, and M. L. Norman (2008), Cosmological shocks in Adaptive Mesh Refinement simulations and the acceleration of cosmic rays, *Astrophys. J.*, *689*, 1063–1077, doi:10.1086/592496.

Vaughan, D. (2008), West Antarctic ice sheet collapse—The fall and rise of a paradigm, *Clim. Change*, *91*, 65–79, doi:10.1007/s10584-008-9448-3.

Vazza, F., G. Brunetti, A. Kritsuk, R. Wagner, C. Gheller, and M. Norman (2009), Turbulent motions and shocks waves in galaxy clusters simulated with adaptive mesh refinement, *Astron. Astrophys.*, *504*, 33–43, doi:10.1051/0004-6361/200912535.

Vialov, S. S. (1958), Regularities of glacial shields movement and the theory of plastic viscous flow, in *Physics of the Motion of the Ice*, *IASH Publ.*, vol. 47, pp. 266–275, IAHS Press, Wallingford, U. K.

Vieli, A., and A. J. Payne (2005), Assessing the ability of numerical ice sheet models to simulate grounding line migration, *J. Geophys. Res.*, *110*, F01003, doi:10.1029/2004JF000202.

R. M. Gladstone, V. Lee, and A. J. Payne, Bristol Glaciology Centre, School of Geographical Sciences, Bristol University, University Road, Bristol BS8 1SS, UK. (r.gladstone@bristol.ac.uk)

A. Vieli, Department of Geography, Durham University, South Road, Durham DH1 3LE, UK.